PRODUCTION AND CHARACTERIZATION OF METAL POWDERS BY ATOMIZATION FOR ADDITIVE MANUFACTURING

Hussain Ali Murtaza, Bachelor of Science

Submitted in fulfillment of the requirements for the degree of Master of Science in Chemical and Material Engineering

School of Engineering and Digital Sciences

Department of Chemical & Materials Engineering

Nazarbayev University

53 Kabanbay Batyr Avenue,

Astana, Kazakhstan, 010000

Supervisor: Prof. Boris Golman

Co-Supervisor: Prof. Asma Perveen

Co-Supervisor: Prof. Didier Talamona

April 28, 2023

DECLARATION

I hereby, declare that this manuscript, entitled “Production and characterization of metal powders by atomization for additive manufacturing”, is the result of my own work except for quotations and citations which have been duly acknowledged.
I also declare that, to the best of my knowledge and belief, it has not been previously or concurrently submitted, in whole or in part, for any other degree or diploma at Nazarbayev University or any other national or international institution.

Name: Hussain Ali Murtaza

Date: 02-05-2023

Acknowledgments

First and foremost, I want to thank my supervisors, Prof. Boris Golman, Prof. Asma Perveen and Prof. Didier Talamona for their guidance and help, as well as for the opportunity to work under their supervision. Secondly, special thanks to the Government of Kazakhstan and NU for providing such a modernized and research-based facility to learn from national and international faculty.

I want to thank Andrei Iankin for helping me in the production of ultrasonic atomized powder AlSi12. Lastly, special and unlimited thanks to my mother and family for providing emotional support to me through my stay in Kazakhstan.

Table of Content

Nomenclature

Parameters	Description
B	parameter in Nukiyama-Tanasawa model
N	number of specimen points
n	spread parameter in Rosin-Rammler model
P	number of independent variables
P	parameter in Nukiyama-Tanasawa model
x_e	scale parameter in Rosin-Rammler model
x_g	geometric mean size in log-normal model
x_m	arithmetic mean size in normal model
σ	standard deviation in normal model
σ_g	geometric standard deviation in log-normal model

Abbreviation

Abbreviation	Description
AIC	Akaike information criterion
$\mathrm{AIC}_{corrected}$	Akaike information criterion corrected
PSD	Particle Size Distribution
$RMSE$	Root mean square error
RSS	Residual sum of squares
SSE	Sum of squared errors

List of Figures

List of Tables

ABSTRACT

The characteristics of the powder used in powder-bed-based additive manufacturing play a significant role in determining both the process conditions and the quality of the parts manufactured. Therefore, it is essential to assess powder characteristics, particularly particle morphology, size distribution (PSD) and rheology. This study aims to characterize the size distribution and morphology of metal powders commonly used in additive manufacturing, such as AlSi10Mg, Inconel-718, Ti6Al4V, titanium, stainless steel and ultrasonic atomized powder AlSi12. The study applies various PSD models to fit the measured volume- and number-based size distributions and conducts a statistical analysis to identify the best-fitting models. Additionally, the study utilizes shape analysis of SEM images based on elliptic Fourier series to quantitatively characterize particle morphology. The study reveals that AlSi10Mg powder exhibits the widest size distribution, while Inconel-718 and stainless steel powders have the narrowest distributions. The ultrasonic atomized AlSi12 powder produced at an angle of 2.5° has the widest particle size dispersion in terms of volume while AlSi12 powder produced at an angle 5° number, according to the data. The narrowest volume- and number-based particle size distributions, however, are shown by AlSi12 powder produced at angle -2.5°and AlSi12 powder produced at angle 0°, respectively. Metal particles, except for AlSi10Mg, are almost spherical, with elongation ratios ranging from 0.90 to 1. AlSI12 exhibit the highest level of sphericity, while AlSi10Mg particles have a rougher surface structure. The Nukiyama-Tanasawa and log-normal distributions fit the experimental PSDs better than the normal and Rosin-Rammler models. Powder rheology tests using FT4 rheometer indicate that AlSi10Mg has the lowest BEF value, resulting in good flowability, Inconel-718 powder forms a denser bed, and titanium has the highest cohesion value and the lowest flow function value, making it the most flowable among all the powders tested. Additionally, we examined the correlations between the powder's rheological properties, measured by a Hall flowmeter, tapped density tester, and FT4 powder rheometer, and the PSD and shape indices using Spearman's coefficient test. The results of this study can assist in selecting the appropriate metal powder for specific additive manufacturing applications.

Chapter 1 - INTRODUCTION

1.1 Introduction

A molten metal stream is broken up into very small droplets during the atomization process, which then solidifies into tiny particles. During World War II, the method was widely employed. By using the above procedure, high-quality powders of aluminium, brass, iron, stainless steel, tool steel, and super alloys are created [1]. Due to the advent of metal additive manufacturing (AM) technology, the need for high-quality metal powder has recently increased significantly[1]. Rapid prototyping and series production using metal AM technologies are becoming more and more common in a variety of industrial fields. The market of metal powder is likely to expand substantially in the upcoming years due to the existing markets in powder metallurgy (P/M) and plasma/thermal spraying as well as the advent of new applications like additive manufacturing.

Most of the applicable additive manufacturing (AM) techniques use mostly powder or wire as a feedstock, which is then selectively melted by a focused heat source and solidified in subsequent cooling to make a product [2], [3]. Making commercial and research-and-development materials for industry involves processing metal powder. Examples of techniques used to create metal powder include gas atomization, plasma atomization, centrifugal atomization, and ultrasonic atomization [4]. Gas atomization process involves disintegrating the flowing stream of molten metal using high-velocity gas. Ar, N2, and He gas jets are the gases used. The powder is atomized and then collected in a water bath. When particular powder characteristics, such as spherical shape or particles with little to no oxide (surface) content, are desired, fluidized bed cooling is used. This method is more expensive than water atomization. Water atomization is the process in which the molten metal stream is disintegrated by high pressure water jets in this process. Water is utilized because of its superior quenching power and increased viscosity. The method is affordable and suitable for both small- and large-scale production. This method cannot atomize metals and alloys that donnot interact chemically with water. With the centrifugal atomization technique, molten metal drops from the consumable electrode's molten end are broken off by centrifugal force. Production of titanium-like reactive metal powders uses this method. This procedure uses a non-consumable tungsten electrode to heat and melts the metal bar's one end while spinning it longitudinally at high speeds [1].
The ultrasonic atomization technique is one way to create high-quality metallic powders. Such powders are used as a starting material for additive manufacturing, powder metallurgy

(sintering), and specialty metallic coatings. Previously, heavy elements and noble metals including platinum, molybdenum, gold, uranium, palladium, and tantalum and its alloys were created using various gas atomization techniques; nevertheless, the quality of the powder generated did not meet all criteria necessary for additive manufacturing, primarily the porosity of the final products [5].

Each of the techniques described produces metal powders with a range of morphology size. Almost all processes result in spherical. The investigation of AM material focuses on its bulk properties, which include tap density, apparent density, compressibility, flow properties, and, as well as, chemical composition. High-quality metal powders are frequently used to create materials for structural and practical purposes. Casting processes and conventional forging are more expensive than the production of metal powder and additive manufacturing [1]. AM needs metal powders to be spherical and have a narrow size distribution in order to deliver repeatable and reliable outcomes. The technologies allow for the creation of powder shapes that are spherical or nearly spherical. Additionally, the results are acquired immediately after powder synthesis, whereas the other methods call for additional processing to produce the best powder form [6].

1.2 Aims and Objectives

The aims of the research is to

- Characterize metal powder (AlSi10Mg, Stainless Steel, Ti, Ti6Al4V, Inconel) used in additive manufacturing.
- Produce metal powder (AlSi12) using ultrasonic atomization.
- Compare commercially produced powder and ultrasonic atomized powder.
- Select particle size distribution models (Normal, Log-Normal, Rosin Rammler, Nukiyama).
- Study rheology of metal powders.

1.3 Literature Review

Powder-based additive manufacturing (AM) is a state-of-the-art technology that enables the production of custom-designed parts. The process involves the layer-by-layer construction of parts by supplying powder to a build chamber, spreading the powder on top of the powder bed using a roller or blade to form the powder layer, and selectively fusing particles using heat or a binder. Metal AM is gaining increasing interest from academia and industries such as aerospace, military, biomedical, and traditional manufacturing [7]–[9]. The rise in demand for

metal AM has led to a surge in studies exploring the complex relationships between the properties of the powder used in 3D printing and the final quality of the manufactured parts [10], [11]. Powder flow and packing characteristics play a crucial role in the process efficiency and final product quality [12]–[14]. Therefore, the quantitative characterization of powder properties is essential for optimizing powder compositions and AM process parameters, reducing the need for multiple, time-consuming, and expensive printing runs[15].

A study was reported in 2021 by Żrodowski.L et al.[5], in which they used a new technique, named ultrasonic atomization for powder production. One of the least investigated processes for atomizing melts is ultrasonic atomization. The internal stresses of melted metal are broken by the acoustic wave rather than by a fast-moving gas or centrifugal force. A ultrasonic tool named as “sonotrode” can be used to inject vibrations directly. This technique is extensively used in the production of aluminum alloy, steel and magnesium alloys, zinc and solders, etc. In his work he characterized well known metal alloys and bulk metallic glasses. Mostly powder particles are spherical in shape of different sizes. Such geometry, which provides adequate tap density and flowability, is essential for both the AM powder bed and the coating.

One research work was done in which two batches of AISI 316L steel powder, one of which was acquired using ultrasonic atomization (UA) and the other through plasma arc gas atomization, were used to create the AM samples that are the subject of this work plasma arc gas atomization(PAGA) [16]. The following inferences could be made in light of the research findings: In the case of UA powder, 92.3% of the total volume of material may be classified between 20 and 63 micrometers, which is a significantly higher percentage than for the PAGA process (usually between 70 to 75 percent for steels). When compared to PAGA, the UA material requires an energy density that is about 15% greater.

Another research was made by Mahdi H et al.[17] In his work, he studied the influence of particle size distribution on metal powder’s flowability, which is essential to numerous additive manufacturing (AM) operations. The production of good standards metal powders, which are spherical in shapes with varied PSDs is made possible by the plasma atomization technology. Six plasma-atomized specimens of Ti-6Al-4V have been characterized with different PSDs [17]. The advantages and disadvantages of different powder techniques are shown in Table 1.

Table 1. 1 Advantages and disadvantages of metal powder produced by different methods

Manufacturing Process	Material	Particle Size Range	Advantages	Disadvantages
Gas Atomization [18]	Ti Alloy	0 -250μm	Suitable for a variety of alloy metals with reactive qualities that come in ingots with a wide range of particle sizes and spherical particles.	Wide particle size Distribution
Water Atomization [19]	Ti Alloy	25-125 μm	The particles are spherical	The feedstock must be in the form of wire or powder, costly
Ultrasonic Atomization [5]	Reactive and Non-reactive metal Alloy	20-120 μm	High quality of Powder output Easy Swap to next material	The feedstock must be in the form of wire or powder, costly,Time

The flowability of powder is determined by various factors, including size, morphology, surface properties, chemical composition and material characteristics of the constituent particles, size distribution and stress state of powder, and ambient temperature and humidity [20]. The packing density of the powder layer in powder-based AM depends on the recoating process and the powder characteristics [21]. The size and shape of metal particles significantly impact their flow and compaction behaviour. Studies have shown that a broader PSD can lead to an increase in packing density, but it also results in reduced flowability [22]–[24]. Moreover, Seyda et al. [25] examined the properties of AM-printed parts using three Ti6Al4V powders with different PSD from various manufacturing processes. They confirmed that simple size distribution characteristics such as median, 10% and 90% particle sizes are insufficient to characterize the relationships between PSD and part properties. It is required to consider the full description of PSD.

Many mathematical models have been proposed to describe the size distribution of particles. The ideal model should accurately reflect the data and be easy to understand and apply to current data. While adding more fitting parameters can improve the model's fit, this can also make the model more complicated and challenging to use with fewer measured points [26]. Bayat et al.[27] conducted a study on 36 PSD models to determine which model best fit experimental soil sample data and, in another study, Colorado-Arango et al.[28] compared six

different PSD models to fit measured data of metallurgical coke grinding products. In the case of metal powder used in AM, some authors use log-normal [29], [30] and Rosin-Rammler [31], [32] distributions to fit measured PSDs. Nevertheless, limited research is available on the comparative analysis of different PSD models for metal powders used in AM. It is essential to determine the most appropriate PSD model, validated by the measured size distribution of metal powder, for effective design and scaling up of powder-based additive manufacturing processes.

The flow behaviour of powder in AM is significantly influenced by its particle morphology [33], [34]. Spherical particles with smooth surfaces are generally considered to have the best flowability [35], whereas non-spherical particles result in lower random packing density [36]. Due to their production method, AM metal particles often deviate from a spherical shape. In this process, pressurized gas or water is used to atomize the molten metal into particles upon cooling. The coalescence of droplets during this process can cause the formation of elongated particles and satellite features on the surface of the primary particle [37].

The correlation between particle morphology and flowability was studied by characterizing the average shape of particles on macro-, meso-, and micro-scales [38]. Shape descriptors were formulated to quantify the form, roundness, and surface texture of the particles. For example, Zhang et al.[39] used eight descriptors to describe the form and roundness of nickel-based superalloy powder. Different approaches were applied to characterize particle surface texture, such as fractal analysis. The shape descriptors based on the elliptic Fourier analysis of particle outlines have also been used in powder technology [40]–[42]. The approach has the advantages of providing various scale shape descriptors and working with particles of any complex outline [43]. However, to the best of our knowledge, this approach has not been applied to the shape characterization of particles used in AM.

Chapter 2 - Materials and Methods

Figure 2.1 shows the process flow for the methods used in the current investigation to examine the size distribution of metal powders, morphology, and rheometer tests for both commercially and ultrasonically atomized powders.

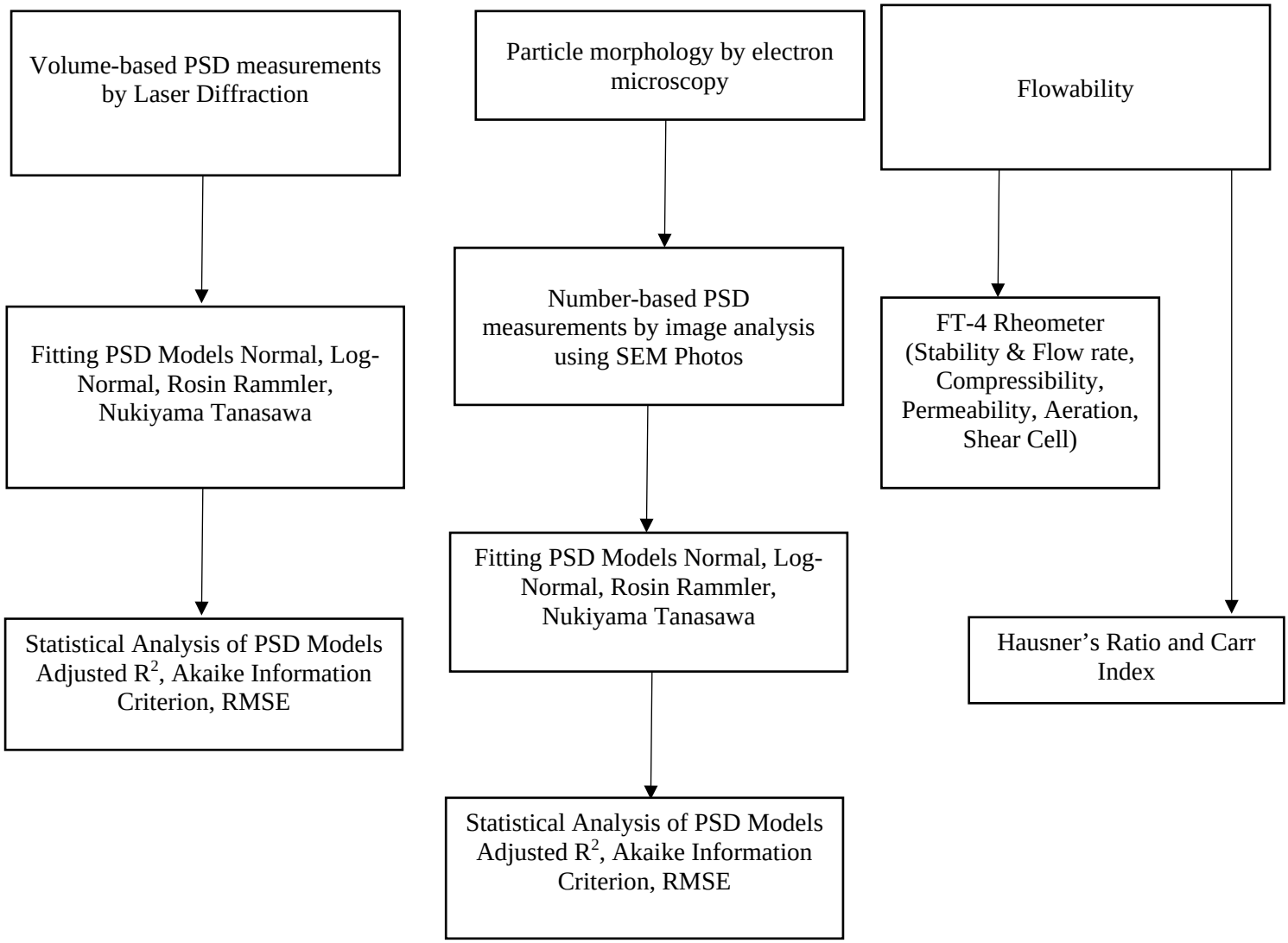

Figure 2.1 Flow chart of study methodology

2.1 Materials

In this research, the size distribution and morphology of five metal powders and AlSI12 powder produced by ultrasonic atomization used in additive manufacturing were studied. The metal powder Inconel-718 and Ti6Al4V were purchased from Sino-Euro Materials Technologies of Xi'an Co.,Ltd., AlSi10Mg from Volgograd Aluminium Company - Powder Metallurgy LLC, titanium from SpetsMetallMaster LLC and stainless steel from POLEMA JSC.

2.2 Production of AlSi12 using Ultrasonic Atomization Process

The method for producing metal powders by ultrasonic atomization includes placing a heavy metal raw material near an electric arc, heating the raw material with the electric arc, and creating a molten metal pool on a sonotrode, the molten metal pool having a temperature equal to or greater than the heavy metal raw material's melting temperature, but less than the heavy metal raw material's vaporization temperature. The metal droplets freely cool down within a preset distance by radiation and transform into a heavy metal powder, collecting the heavy metal powder, at the end 75% of the heavy metal raw material is collected in the form of the heavy metal powder. The flow process is shown in figure 2. 2.

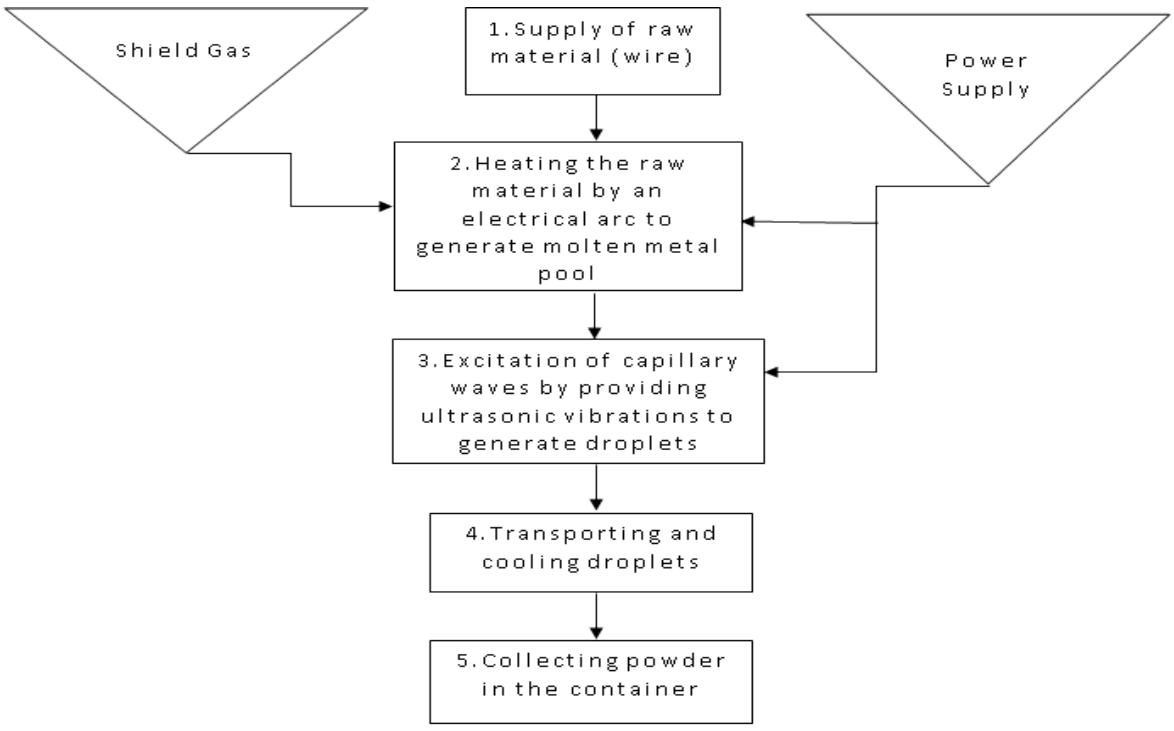

Figure 2.2 Production of metal powder using ultrasonic atomization

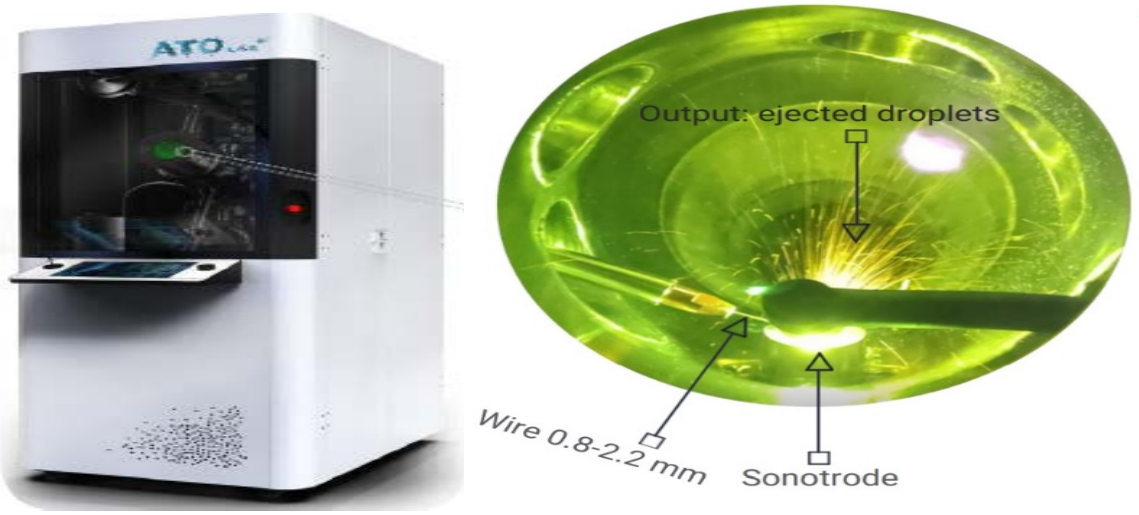

Figure 2.1 Ultrasonic atomizer

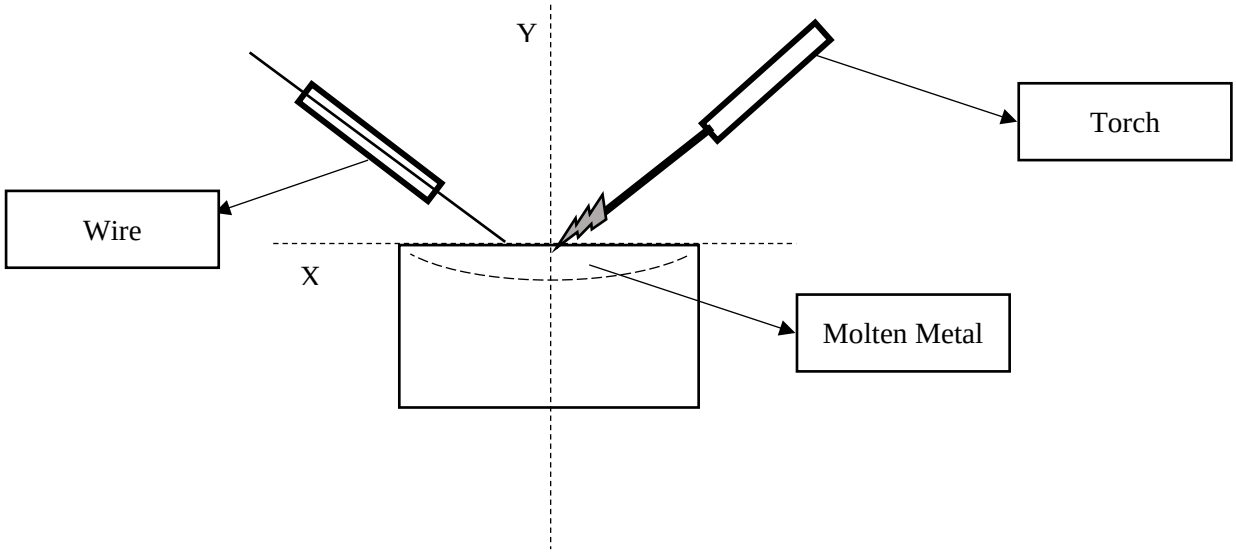

Figure 2.2 Melting of wire on sonotrode

Table 2.1 Parameter for producing AlSi12 powder

Material	Electrical current, A	Ultrasonic vibration amplitude, %	Ultrasonic vibration frequency, kHz	Main circuit pump flow, %	Argon flow, l/min	Feed Rate
AlSi12	140 A	80	35	55	10	10-15%

If the flow of argon is less than 10 l/min, we cannot start the ignition process. So it should be 10 l/min or more. Feed rate for the machine is 10 to 15%, whereas it might reach 30% for the other machine. Table 2.1 displays the production parameters for AlSi12.

2.3 Measurement Techniques

The metal particles were examined using a high-resolution scanning electron microscope (SEM, JSM-IT200 (LA), JEOL Ltd.), which was operated at a beam energy of 5 kV. To prepare a sample for analysis, a copper film was used to cover the sampling stage instead of the commonly used carbon tape. This was done to provide a distinct background in the pictures, making it easier to distinguish particles. The powder was evenly distributed in small amounts to prevent the overlap of particles in images. A thin 5 nm gold coating was deposited on particles before imaging.

The laser diffraction technique was employed to measure the volume-based size distributions of metal particles using a Mastersizer-3000 particle size analyzer equipped with an Aero S dried powder disperser (Malvern Panalytical, Malvern). The measurements were performed using the dry method, where the powder was dispersed in the measuring cell with compressed air at a pressure of 1 to 1.5 bar. To account for differences in the flowability of the samples, the powder feed rate was adjusted from 25% to 100%. The refractive index of the metal powders, AlSi10Mg, Inconel-718, stainless steel, titanium, AlSi12 and Ti6Al4V, was set to 1.78, 1.96, 2.76, 2.15, 1.78 and 2.51, respectively. The absorption index was set at 6.5, 2.07, 1.06, 1.41,6.5, and 1.413, respectively.

The outline, area, and Ferret diameter of metal particles were detected on SEM photographs using image analysis in the open-source ImageJ software [44]. The number-based PSD was estimated based on the Ferret diameter for AlSi10Mg and the equivalent circle diameter for all other powders.

2.4 Shape Analysis

In this study, we utilized the elliptic Fourier analysis of particle outlines to derive the shape indices. The particle outlines were detected in SEM photographs of metal particles using ImageJ software. The outline of each particle was traversed and sampled at equal intervals along the outline length. The coordinates of outline points, denoted as $P_{x,i}, P_{y,i}$, were saved at every incremental step angle $\theta_i = 2\pi i/N$, where N represents the number of divisions of the particle outline. The closed outline $(x(\theta), y(\theta))$ was approximated using elliptic Fourier series expressed as follows [45]–[47]:

$$\begin{aligned} x(\theta_i) &= a_{x,0} + \sum_{j=1}^{M} a_{x,j} \cdot \cos(j\theta_i) + b_{x,j} \cdot \sin(j\theta_i), \\ y(\theta_i) &= a_{y,0} + \sum_{j=1}^{M} a_{y,j} \cdot \cos(j\theta_i) + b_{y,j} \cdot \sin(j\theta_i), \end{aligned} \tag{1}$$

where $a_{x,j}, b_{x,j}, a_{y,j},$ and $b_{y,j}$ are the Fourier cosine/sine coefficients for the functions *x* and *y*, respectively, and M denotes the number of harmonics in the Fourier series.

The coefficients were calculated as follows:

$$a_{x,j} = \frac{2}{N}\sum_{i=0}^{N-1} P_{x,i}\ \cos\left(\frac{2\,\pi\,i\,j}{N}\right),\quad a_{y,j} = \frac{2}{N}\sum_{i=0}^{N-1} P_{y,i}\ \cos\left(\frac{2\,\pi\,i\,j}{N}\right),$$
$$b_{x,j} = \frac{2}{N}\sum_{i=1}^{N-1} P_{x,i}\ \sin\left(\frac{2\,\pi\,i\,j}{N}\right),\quad b_{y,j} = \frac{2}{N}\sum_{i=1}^{N-1} P_{y,i}\ \sin\left(\frac{2\,\pi\,i\,j}{N}\right). \tag{2}$$

The particle shape indices at both the macro- and micro-scales were evaluated using Fourier series coefficients. The macro-scale index, denoted as the elongation ratio *K*, was defined as a ratio of minor $r_{el,s}$ to major $r_{el,l}$ radii of the approximated ellipse :

$$K = \frac{r_{el,s}}{r_{el,l}}, \tag{3}$$

The radii of the approximated ellipse were calculated using the second Fourier coefficients $a_{x,1}, b_{x,1}, a_{y,1},$ and $b_{y,1}$ as follows:

$$r_{el,l} = (B\cdot C - A\cdot D)\,/\sqrt{C^2 + D^2}\,, r_{el,s} = (B\cdot C - A\cdot D)\,/\sqrt{A^2 + B^2},$$
$$A = a_{x,1}\,cos(\beta) + a_{y,1}\,sin(\beta);\ B = b_{x,1}\,cos(\beta) + b_{y,1}\,sin(\beta),$$
$$C = a_{y,1}\,cos(\beta) - a_{x,1}\,sin(\beta);\ D = b_{y,1}\,cos(\beta) - b_{x,1}\,sin(\beta), \tag{4}$$
$$\beta = -\frac{1}{2}\tan^{-1}\left\{\frac{2\left(a_{x,1}\cdot a_{y,1} + b_{x,1}\cdot b_{y,1}\right)}{a_{y,1}^2 + b_{y,1}^2 - a_{x,1}^2 - b_{x,1}^2}\right\}$$

The micro-scale shape index, referred to as the surface roughness $C_{v,rs}$, was defined based on the coefficient of variation of the distance from the centroid of particle outline:

$$C_{v,rs} = \frac{\sqrt{\frac{1}{N}\sum\left(R\ (\theta_i) - r_{el}(\theta_i)\right)^2}}{r_c}. \tag{5}$$

Here, $R\ (\theta_i)$ and $r_{el}(\theta_i)$ denote the radii of the outline point and equivalent ellipse at an angle θ_i, respectively, and r_c is the radius of the circle that has the same perimeter as the approximated ellipse. They were calculated as

$$R(\theta_i)\ = \sqrt{P_{x,i}^2 + P_{y,i}^2},\qquad r_{el}(\theta_i)\ = r_{el,l}\,r_{el,s}/\sqrt{r_{el,l}^2 - \left(r_{el,l}^2 - r_{el,s}^2\right)cos^2(\theta_i)},$$
$$r_c = \frac{2\,r_{el,l}}{\pi}\int_0^{\frac{\pi}{2}}\sqrt{1 - \left[1 - \frac{r_{el,s}^2}{r_{el,l}^2}\right]sin^2(\theta_i)}\ d\theta \tag{6}$$

2.5 Flowability measurement using FT-4 measurement:

The rheological properties of powders is meant to be evaluated more precisely using an FT4 powder rheometer since it is more sensitive than the relatively crude funnel-based procedures. There are several testing modes available to assess the behavior of the powder under various circumstances, and each mode offers some new information about the rheology of the powder. The documentation and publications of the manufacturer can be consulted for a thorough description of the testing modes that are offered as well as a comprehensive list of the software outputs for FT4 powder rheometers. Five testing modes, including dynamic flow, aeration, permeability, compressibility, and shear testing modes, were chosen for this investigation. These testing modes are briefly presented in the paragraphs that follow.

Figure 2.3 Ft-4 Rheometer

Procedure for testing flow rate and stability: The stability and flow rate test is often a series of adjustments and tests cycles designed to determine whether the flow will cause the powder to alter.

- In the stability and flow rate test, the powder forms of Basic flow energy(BFE), specific energy(SE), and Conditioned Bulk Density(CBD) were looked at. When the blades are moving downward, BFE is qualitatively measured. As the blade rotates upward, the SE determines the flowability of the powder during low-shear blending. The powder was poured into the testing apparatus and gently shifted to release and aerate into a uniformly packed power bed, free of extra air, in order to determine the CBD.
- The air in the powder significantly affects the flow characteristics. The purpose of the aeration test is to determine how differently the powder samples move before and after air is added. This test gives a measure of the adhesion strength to describe the powder's blending, aerodynamics, and fluid motion.
- Compressibility testing measures how much a sample's volume changes under various conditions of normal stress, and the results of this experiment show how well the sample performed overall. The findings demonstrate that the powder is compressed under a typical stress, and the volume change brought on by storage, transit, direct pressure, and rolling is measured.

- The gas permeability test depends on the compressibility test, which involves filling the powder with a specific amount of air and measuring the pressure drop of the gas that passes through the powder as the normal stress changes. The powder's air permeability decreases with pressure drop and increases with pressure drop, respectively.

- A vented piston compacted the powder until the desired consolidation stress was reached and measured in order to determine the cohesive index. We use a 25 mm x 10 mL vessel to conduct the test.

2.6 Particle Size Distribution Models

In the present work, we evaluated the normal, log-normal, and Rosen-Rammler models, commonly used to describe the powder size distribution, as well as the Nukiyama-Tanasawa model to fit the measured PSDs of metal powder. Nukiyama and Tanasawa[48] developed an empirical equation to fit the size distribution of droplets generated by atomizing liquids with twin-fluid nozzles.

The cumulative undersize distribution, *D*, according to the normal PSD model, is given by [49]

$$D(x) = \frac{1}{2}\left(1 + \text{erf}\left(\frac{x - x_m}{\sqrt{2}\ \sigma}\right)\right), \tag{7}$$

where x is the particle size and $\text{erf}\,(z)$ is the error function of $z = \frac{x - x_m}{\sqrt{2}\ \sigma}$. The error function is defined as

$$\text{erf}(z) = \frac{2}{\sqrt{\pi}} \int_0^z \exp(z^{-2})\ dz. \tag{8}$$

The normal PSD model has two parameters: the arithmetic mean size, x_m, which represents the central tendency of the distribution, and the standard deviation, σ, which relates to the width of the distribution. Equation (7) can be transformed into a linear form:

$$Y = aX + b, \tag{9}$$

where $X = \ \text{erf}^{-1}(2D - 1)$, $\text{erf}^{-1}(z_1)$ is the inverse error function of $z_1 = 2D - 1$, and $Y = x$. The model parameters x_m and σ can be calculated from the line intercept *b* and the line slope *a* as follows: $x_m = b$ and $\sigma = a/\sqrt{2}$ ·

The cumulative undersize distribution function for the log-normal particle size distribution (PSD) model is given by the following equation [50, pp. 57–58]:

$$D(x) = \frac{1}{2}\left(1 + \mathrm{erf}\left(\frac{\ln x \ - \ln x_g}{\sqrt{2}\ \ln \sigma_g}\right)\right) \tag{10}$$

The log-normal model is characterized by its geometric mean size x_g and geometric standard deviation σ_g, which are estimated by linear fitting of the measured undersize distributions. The fitting process involves transforming the measured data into a linear form, with the abscissa given as $X = \ \mathrm{erf}^{-1}(2D - 1)$ and the ordinate as $Y = \ln x$. The model parameters can then be calculated from the slope ($a = \sqrt{2}\ \ln \sigma_g$) and intercept ($b = \ln \sigma_g$) of the fitted line.

The Rosin-Rammler PSD model is expressed in cumulative form as follows [51]:

$$D(x) = 1 - \exp\left\{-\left(\frac{x}{x_e}\right)^n\right\}, \tag{11}$$

where x_e represents the scale parameter of the distribution and n ($n > 0$) denotes the spread parameter which controls the width of the distribution, with higher values of n indicating a narrower distribution. The Rosin-Rammler PSD model can be transformed into a linear form by Eq. (9) with $X = \ln x$ and $Y = \ln\left[\ln\left(\frac{1}{1-D}\right)\right]$. This transformation provides the slope $a = n$ and the intercept $b = -n \ln x_e$ of the best-fit line, which can then be used to estimate the model parameters x_e and n.

The cumulative undersize distribution according to the Nukiyama-Tanasawa PSD model is given as [52]:

$$D(x) = 1 - \Gamma\left(\frac{p+1}{c}, b \times D^c\right) / \Gamma\left(\frac{p+1}{c}\right), \tag{12}$$

where $\Gamma(z_2)$ denotes the gamma function of $z_2 = (p+1)/\mathrm{c}$ and $\Gamma(z_2, z_3)$ represents the incomplete gamma function of z_2 and $z_3 = b \times D^c$. The gamma and incomplete gamma functions are defined as [53]:

$$\Gamma(z_2) = \int_0^\infty t^{z_2 - 1}\, \mathrm{e}^{-t}\, dt, \Gamma(z_2, z_3) = \int_{z_3}^\infty t^{z_2 - 1}\, \mathrm{e}^{-t}\, dt. \tag{13}$$

The values of the adjustable parameters b and p are estimated through the nonlinear fitting of measured size distributions, and the value of parameter c is fixed at $c = 1$.

2.7 Statistical Analysis

The effectiveness of the PSD models was evaluated using three statistical indices: adjusted R^2, Akaike's information criterion corrected, and Root Mean Square Error (RMSE) [54]. The adjusted R^2 was used to estimate the difference between the measured and predicted by model PSD values. The Akaike information criterion (AIC) was employed to compare the

fitting quality of different models. The residual errors were evaluated with the help of the root mean of squared error.

The adjusted R^2 is calculated as

$$R^2_{\text{adjusted}} = R^2 - \frac{(1 - R^2)k}{N - k - 1}, \tag{14}$$

where *N* denotes the number of PSD data points and *k* stands for the number of parameters.

The Akaike information criterion is expressed as follows:

$$AIC = N \cdot \ln\left(\frac{SSE}{N}\right) + 2k, \tag{15}$$

where *SSE* is the sum of squares due to error, $\boldsymbol{SSE} = \sum_{i=1}^{N}(\boldsymbol{D_i^{exp}} - \boldsymbol{D_i^{cal}})^2$, $\boldsymbol{D_i^{exp}}$ and $\boldsymbol{D_i^{cal}}$ denote the experimental and predicted by model cumulative undersize distributions, respectively.

The AIC corrected index is used if there are fewer than 40 data set points. [41]

$$AIC_{corrected} = AIC + \frac{2k(k+1)}{N - k - 1}. \tag{16}$$

The root mean square error is expressed as

$$RMSE = \sqrt{SSE/N}. \tag{17}$$

2.8 Measurement of bulk density and tapped density

The methodology was developed for measurements of apparent bulk density using the Hall flowmeter. Firstly, measure the weight of empty cup of hall flow meter. Then, fill the funnel with powder, then let it exit through the density cup orifice. In the end, level the surface of density cup and measure the cup weight. The methodology was developed for measurements of tapped density using tapped density meter. Weigh an appropriate quantity of the powder sample utilizing an analytical balance. Place the sample in the sample holder of the tap density meter and note its height so that it aligns with the holder's top. Start the tap density measurement by turning on the tap density meter. Record the volume readings after each tap until they stabilize. Adjust the tapping number to 1000. After tapping the powder, press calculate in the machine to get tapped density. Finally, clean the sample holder and the tap density meter in preparation for the following measurement. These bulk and tapped density are useful for calculating the Hausner's ratio and Carr's index for flowability measurements.

Chapter 3- Results and Discussions

3.1 Morphology of metal powders

3.1.1 SEM images of commercially produced powders

Five different metal powders are shown in the SEM image of commercially produced metal powders in Fig. 3.1, with the AlSi10Mg particles appearing non-spherical while the other four are nearly spherical.

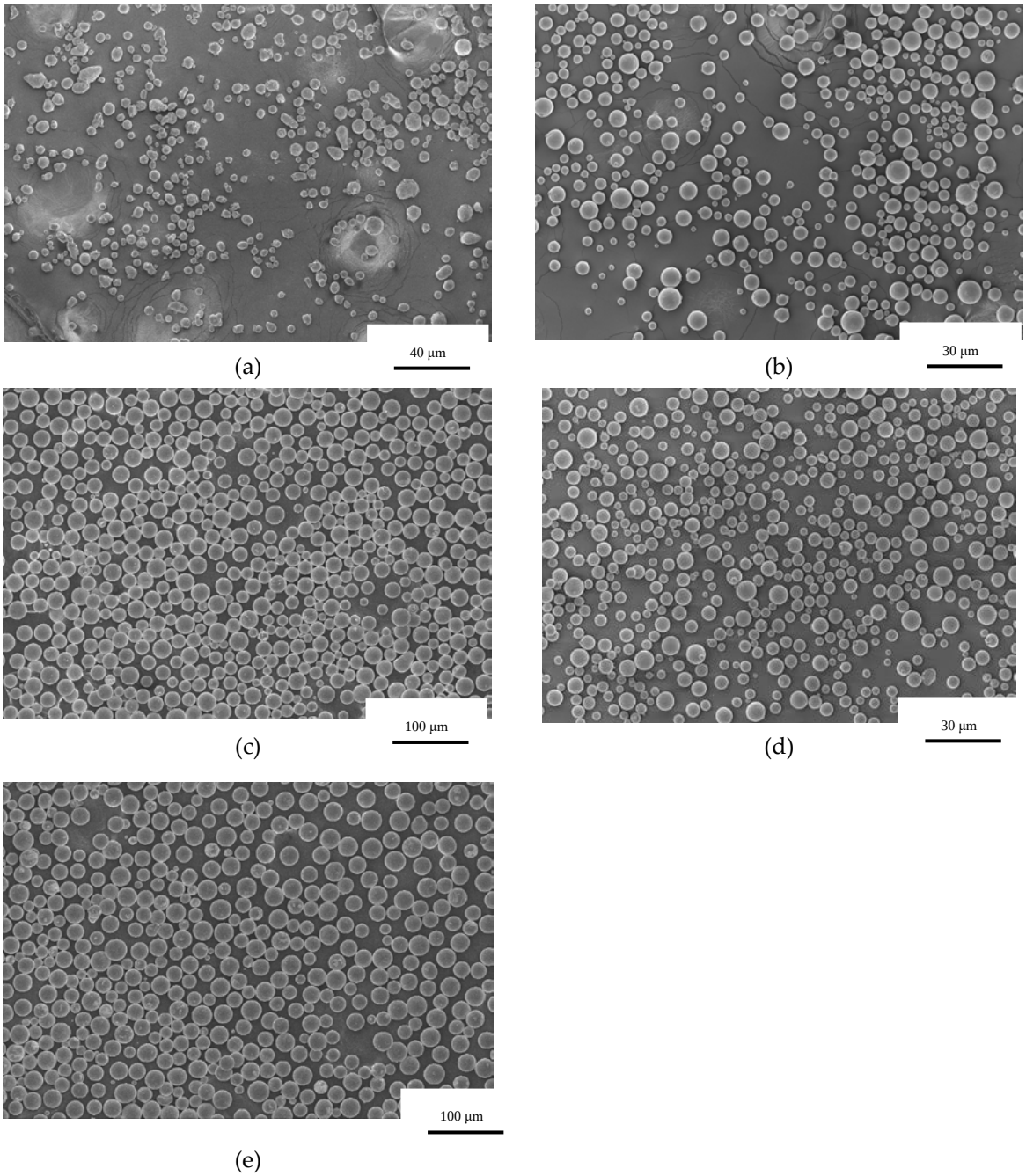

Figure 3.1 SEM images of metal powder: (a) AlSi10Mg, (b) Ti6Al4V, (c) Inconel-718, (d) Ti (e) stainless steel.

3.1.2 SEM images of ultrasonic atomized produced powder

SEM images of AlSi12 ultrasonic atomized produced at different angles (0,2.5, -2.5,5, -5) of manipulator are shown in figure 3.2. All powders are spherical in shape. AlSi12 (ultrasonic atomized) have more spherical particles than AlSi10Mg (gas atomized).

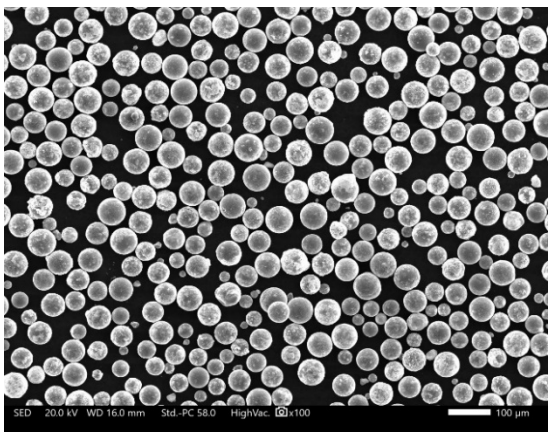

(a)

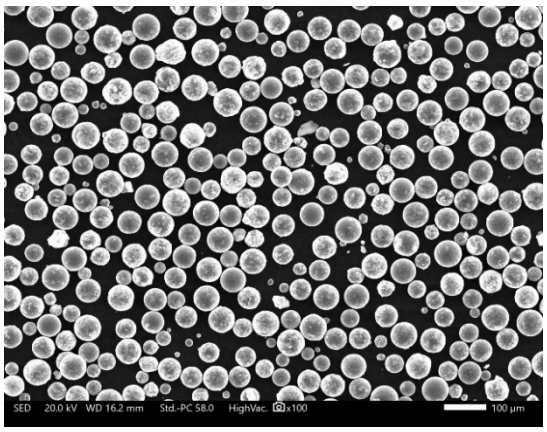

(b)

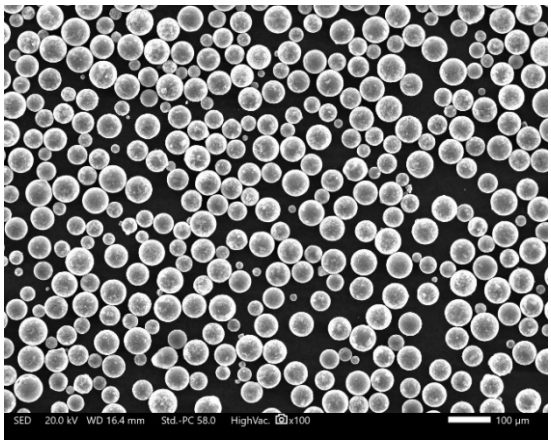

(c)

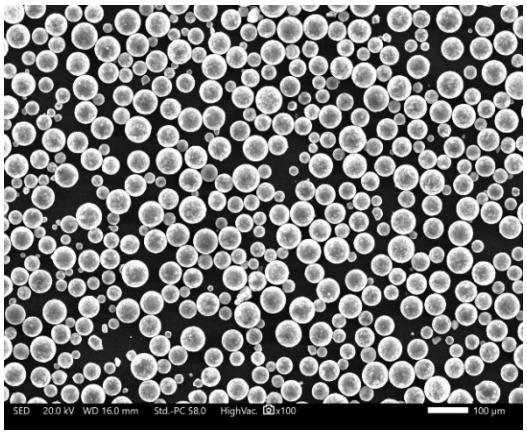

(d)

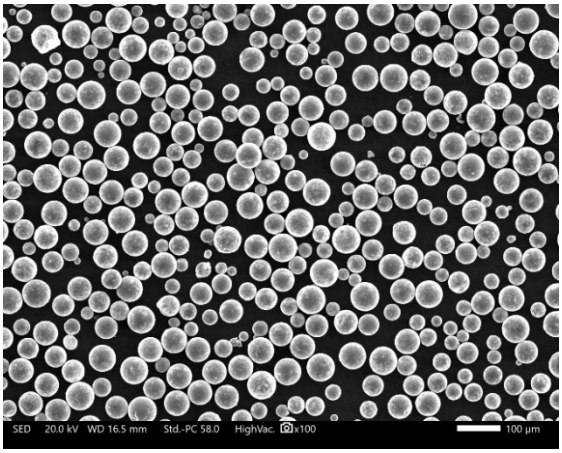

(e)

Figure 3.2 SEM images of metal powder: (a) AlSi12(0°), (b) AlSi12(2.5°), (c) AlSi12(-2.5°), (d) AlSi12(5°) and (e) AlSi12(-5°).

Table 3.1 The mode, median and span of volume-based size distributions of metal particles.

Metal particles	Mode	Median, µm	Span
AlSi10Mg	37.70	36.20	0.98
Inconel-718	33.20	31.44	0.41
Stainless steel	33.20	31.52	0.72
Titanium	29.25	26.50	0.82
Ti6Al4V	33.20	30.73	0.88

3.2 Particle size distribution analysis of metal powders

3.2.1 Particle size distribution analysis of commercially produced powders.

Figure 3.3 (b) shows the volume-based frequency distribution of metal powders as determined by laser diffraction, and Figure 3.3 (a) displays the cumulative distribution (b). Table 3.1 provides a summary of the properties of the size distributions, including the mode, median, and span. The median (D50) is computed as the point that divides the distribution into two halves, with 50% of the particles being smaller and 50% being larger. The mode of the distribution is defined as the highest point in the frequency distribution function. The ratio of (D90 - D10) to D50, where D10 and D90 are the 10th and 90th percentiles of the cumulative undersize distribution, respectively, determines the span of the distribution.

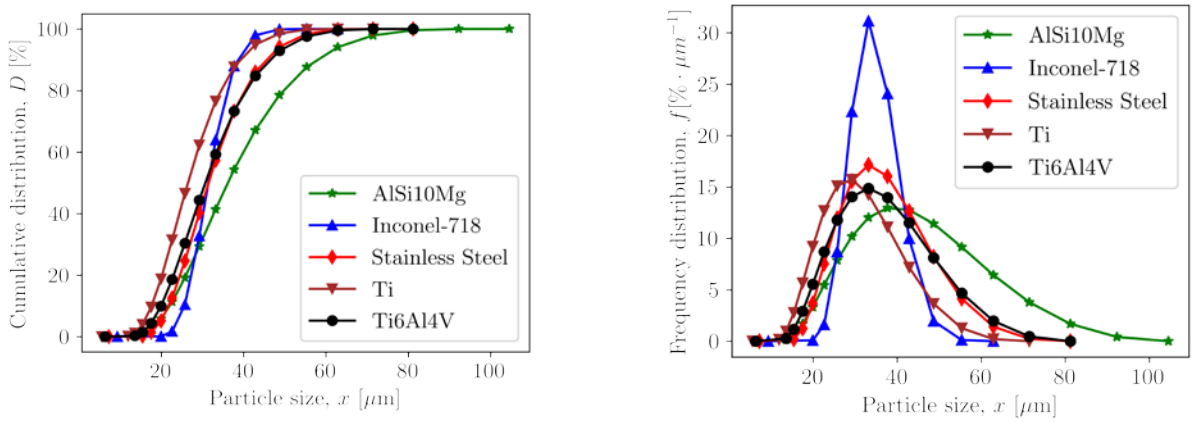

(**a**) (**b**)

Figure 3.3 Measured volume-based (a) cumulative and (b) frequency size distributions of metal powder

The number-based frequency distribution of metal powders is illustrated in Fig. 3.4 (a) and the cumulative distribution is shown in Fig. 3.4 (b). The mode, median and span of size distributions based on number are summarized in Table 3.2.

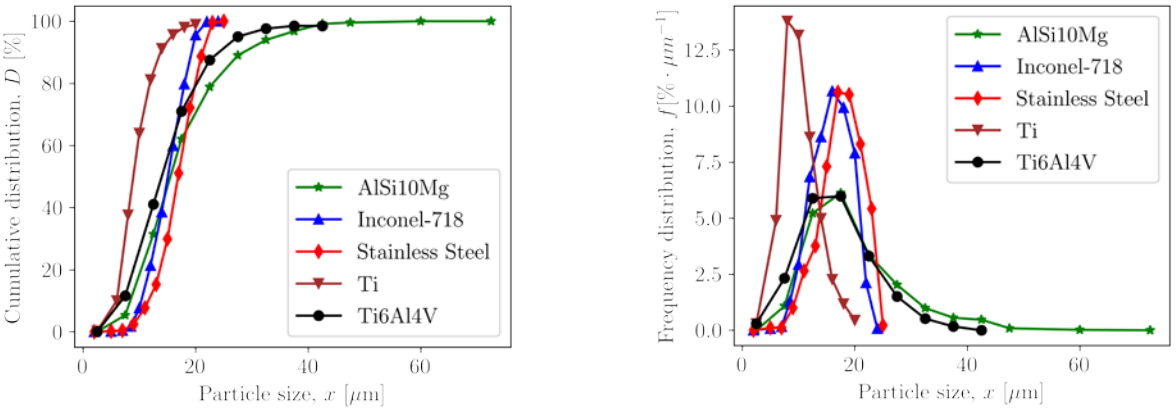

(**a**) (**b**)

Figure 3.4 Measured number-based (a) cumulative and (b) frequency size distributions of metal powder.

Table 3.2 The mode, median, and span of number-based size distributions of metal particles

Metal particles	Mode	Median, µm	Span
AlSi10Mg	17.50	15.53	1.30
Inconel-718	16.00	15.07	0.59
Stainless steel	17.00	16.90	0.57
Titanium	8.00	8.93	0.87
Ti6Al4V	17.5	13.99	1.24

AlSi10Mg has the widest particle size dispersion in terms of volume and number, according to the data shown in Fig. 3.4 and Table 3.2. It also has the biggest median size based on volume and the second biggest median size based on number. The narrowest volume- and number-based particle size distributions, however, are shown by stainless steel and Inconel-718, respectively. The median sizes are also the smallest for titanium powder.

3.2.2 Particle Size Distribution analysis of ultrasonic atomized produced powder

Figure 3.5 (b) shows the volume-based frequency distribution of metal powders AlSi12 as determined by laser diffraction, and Figure 3 (a) displays the cumulative distribution (b). Table 3.3 provides an overview of the mean, median, and range of size distributions based on volume. Table 3.3 provides a summary of the properties of the size distributions, including the mode, median, and span.

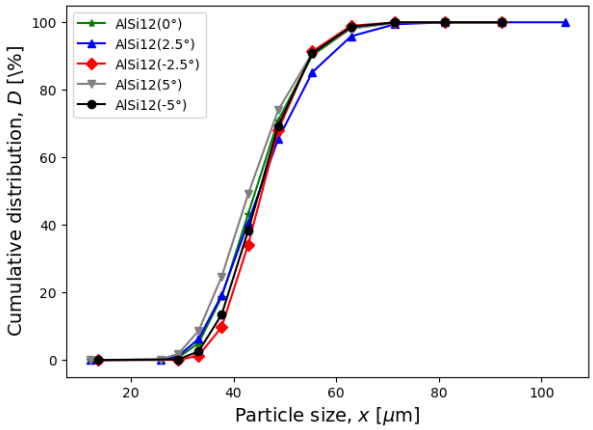

(**a**)

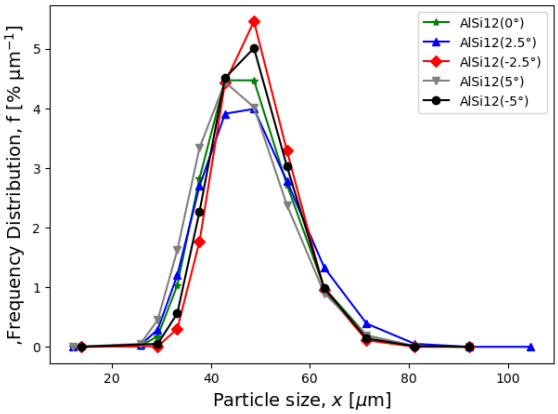

(**b**)

Figure 3.5 Measured volume-based ultrasonic atomized powder AlSi12 at a different angle of the manipulator (a) cumulative and (b) frequency size distributions of metal powder

Table 3.3 The mode, median and span of volume-based size distributions of metal particles.

Metal particles	Mode	Median, μm	Span
AlSi12(0°)	48.70	45.28	0.40
AlSi12(2.5°)	48.70	45.05	0.54
AlSi12(-2.5°)	48.70	45.59	0.38
AlSi12(5°)	48.70	43.04	0.43
AlSi12(-5°)	48.70	45.06	0.42

The number-based frequency distribution of metal powders is illustrated in Fig. 3.6 (b) and the cumulative distribution is shown in Fig. 3.6 (a). The mode, median, and span of size distributions based on number are summarized in Table 3.4.

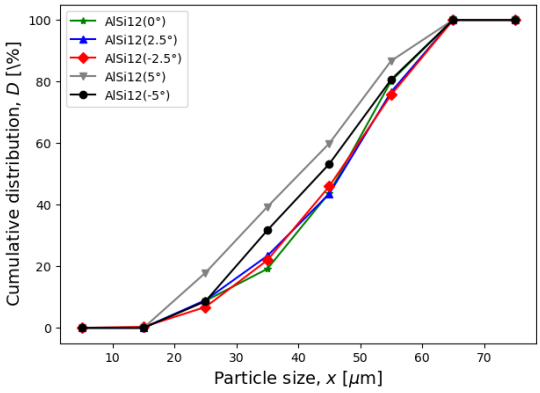

(**a**)

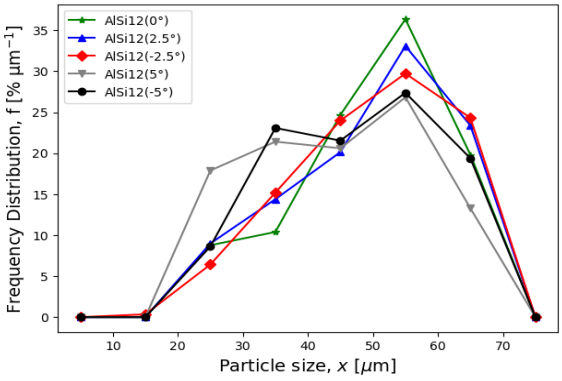

(**b**)

Figure 3.6 Measured number-based ultrasonic atomized powder AlSi12 at a different angle of the manipulator (a) cumulative and (b) frequency size distributions of metal powder

Table 3.4 The mode, median and span of number-based size distributions of metal particles.

Metal particles	Mode	Median, μm	Span
AlSi12(0°)	55.00	46.70	0.72
AlSi12(2.5°)	55.00	46.96	0.75
AlSi12(-2.5°)	55.00	46.36	0.73
AlSi12(5°)	55.00	40.20	0.92
AlSi12(-5°)	55.00	43.50	0.79

The ultrasonic atomized AlSi12 powder produced at an angle of 2.5° has the widest particle size dispersion in terms of volume while AlSi12 powder produced at an angle 5° in term of number, according to the data shown in Fig. 3.5 and Table 3.3. The narrowest volume- and number-based particle size distributions, however, are shown by AlSi12 powder produced at angle -2.5°and AlSi12 powder produced at angle 0°, respectively.

3.3 Shape Analysis

3.3.1 Shape analysis of commercially produced powders

Figure 3.7 illustrates the distributions of the elongation ratio and surface roughness of commercially metal particles that were measured by image analysis. Table 3.5 summarizes the characteristics of the shape index distributions, such as mode, median, and interquartile range. The interquartile range (IQR) indicates the spread of shape indices and is calculated as the difference between the 90th and 10th percentiles of the distribution.

Most metal particles, with the exception of AlSi10Mg, have an elongation ratio (ER) ranging from 0.90 to 1, indicating a spherical shape and a median ER greater than 0.96. Inconel-718 particles show the highest level of sphericity, with a median ER of 0.99 and a narrow ER distribution. Alumina alloy particles exhibit the broadest range of ER, indicating the presence of particles with varying shapes. This observation is supported by the analysis of SEM photographs in Figure 1(a), which confirms the existence of agglomerated particles with elliptical and bulky shapes. In addition, the AlSi10Mg particles demonstrate the roughest surface structure, as evidenced by the high median value of the $C_{v,rs}$ index. In contrast, Ti particles have the smoothest surface, with the lowest median surface roughness.

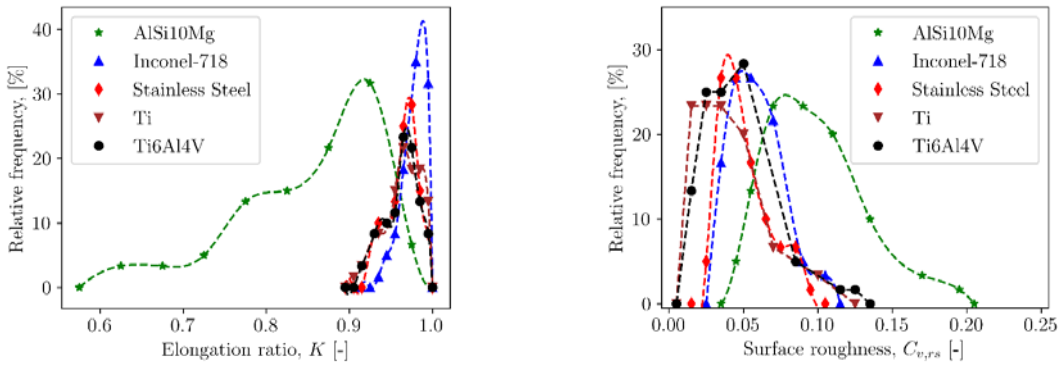

(a) (b)

Figure 3.7 Measured (a) elongation ratio and (b) surface roughness distributions of metal particles.

Table 3.5 The mode, median and IQR of shape index distributions of metal particles

Metal powder	Elongation ratio			Surface roughness		
	Mode	Median	IQR	Mode	Median	IQR
AlSi10Mg	0.925	0.848	0.175	0.0800	0.0771	0.0738
Inconel-718	0.965	0.990	0.0413	0.0500	0.0475	0.0378
Stainless steel	0.975	0.966	0.0480	0.0400	0.0419	0.0456
Titanium	0.965	0.965	0.0605	0.0250	0.0264	0.0407
Ti6Al4V	0.965	0.962	0.0568	0.0500	0.0297	0.0366

3.3.2 Shape analysis of ultrasonic atomized produced powders

Figure 3.8 illustrates the distributions of the elongation ratio and surface roughness of metal particles (AlSi12) that were measured by image analysis. Table 3.6 summarizes the characteristics of the shape index distributions, such as mode, median, and interquartile range. The interquartile range (IQR) indicates the spread of shape indices and is calculated as the difference between the 90th and 10th percentiles of the distribution.

Most metal particles of AlSi12, have an elongation ratio (ER) ranging from 0.90 to 1. AlSi12 particles produced at angle -5 show the highest level of sphericity, with a median ER of 0.99 and a narrow ER distribution. This observation is supported by the analysis of SEM photographs in Figure 3.2.

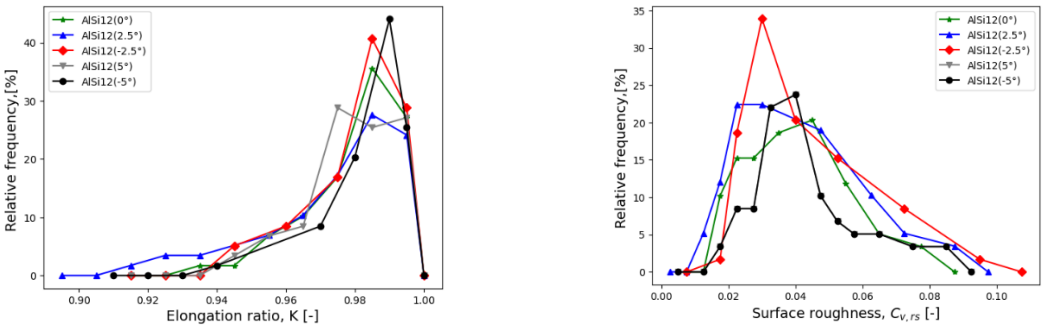

(a) (b)

Figure 3.8 Measured (a) elongation ratio and (b) surface roughness distributions of metal particles.

Table 3.6 The mode, median and IQR of shape index distributions of metal particles

	Elongation ratio			Surface roughness		
Metal powder	Mode	Median	IQR	Mode	Median	IQR
AlSi12(0°)	0.979	0.985	0.037	0.0313	0.0450	0.0363
AlSi12(2.5°)	0.976	0.985	0.053	0.0260	0.0300	0.0460
AlSi12(-2.5°)	0.980	0.985	0.038	0.0291	0.0301	0.0332
AlSi12(5°)	0.976	0.975	0.037	0.0349	0.0400	0.0389
AlSi12(-5°)	0.984	0.990	0.024	0.0349	0.0400	0.0389

3.4 Particle size distribution fitting models and statistical analysis

3.4.1 Particle size distribution fitting Models for commercially produced powder

Figure 3.9 shows the fitting of the volume-based size distributions of metal particles (commercially produced) to normal, log-normal, Rosin-Rammler, and Nukiyama-Tanasawa PSD models. Table 3.7 provides a summary of the parameters that suit each metal powder and model type the best. It can be seen that compared to the normal and Rosin-Rammler distribution models, the Nukiyama-Tanasawa and log-normal distributions show a better fit to the experimental data.

Figure 3.10 shows how PSD models were used to match the measured number-based size distributions of metal powders. Table 3.8 compiles the matching best-fitted model parameters. The Nukiyama-Tanasawa model is best suited to describe the PSDs of Ti6Al4V, Inconel-718, and stainless steel powders, according to the visual observations, whereas the log-normal model is a good match for the number-based PSD of AlSi10Mg and Ti powders. To confirm this conclusion, the adjusted coefficients of determination, root mean square errors, and

corrected AIC metrics are compared for PSD models.

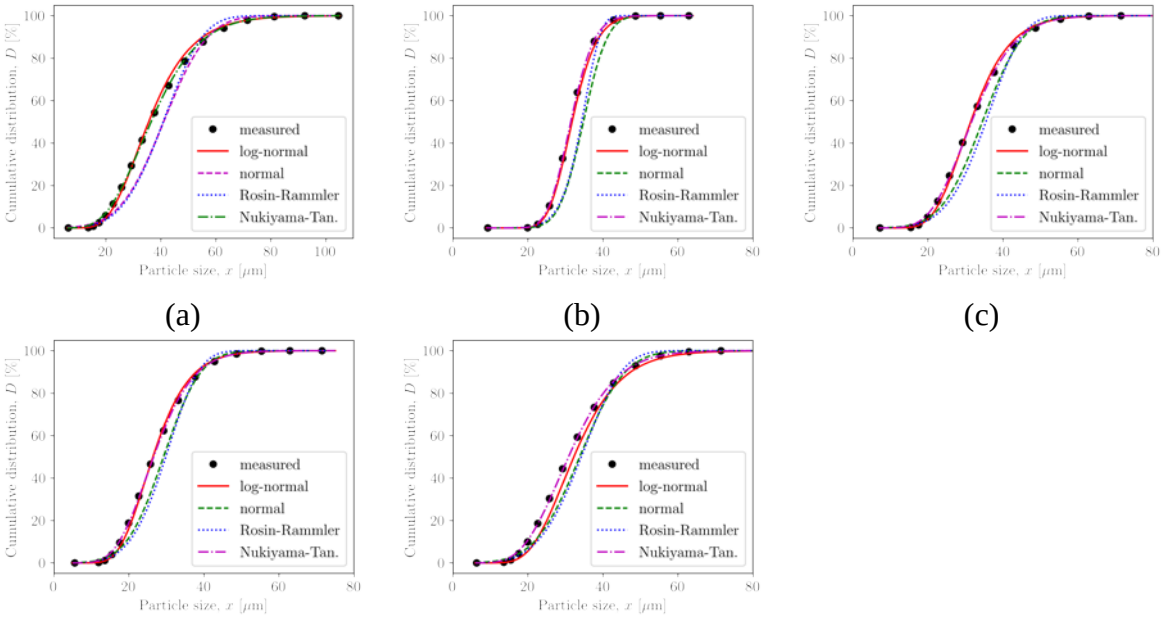

Figure 3.9 Fitting of volume-based PSDs with normal, log-normal, Rosin-Rammler and Nukiyama-Tanasawa distributions: (a) AlSi10Mg, (b) Inconel-718, (c) stainless steel, (d) Ti, (e) Ti6Al4V.

Table 3.7 Parameters of best-fitted volume-based PSD models.

Metal powder	Normal		Log-normal		Rosin-Rammler	Nukiyama		
	x_m	Σ	x_g	σ_g	x_e	N	B	P
AlSi10Mg	41.02	12.53	35.59	1.41	44.77	4.03	0.20	6.47
Ti	29.26	7.81	26.43	1.33	32.26	4.71	0.39	9.78
SS	34.53	8.61	31.41	1.30	38.11	5.09	0.39	11.73
Ti6Al4V	33.84	9.49	32.28	1.35	37.20	4.44	0.30	8.67
Inconel	34.80	5.05	31.80	1.17	35.74	9.28	1.30	40.14

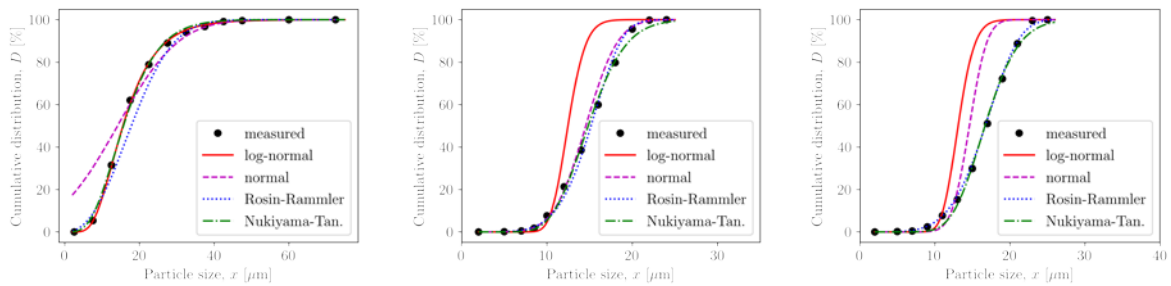

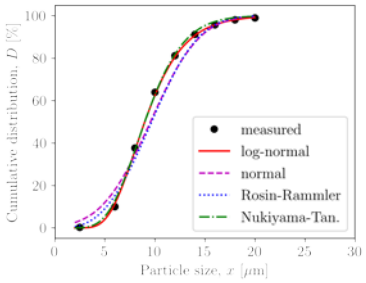

(d)

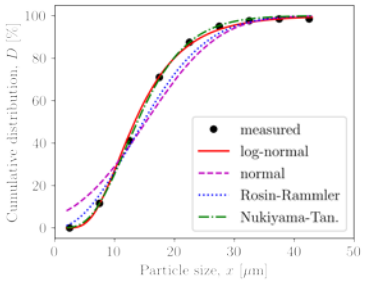

(e)

Figure 3.10 Fitting of number-based PSDs with normal, log-normal, Rosin-Rammler and Nukiyama Tanasawa distributions: (a) AlSi10Mg, (b) Inconel-718, (c) stainless steel, (d) Ti, (e) Ti6Al4V.

Table 3. 8 Parameters of best-fitted number-based PSD models.

Metal powder	Normal		Log-normal		Rosin-Rammler		Nukiyama	
	x_m	Σ	x_g	σ_g	x_e	N	b	p
AlSi10Mg	14.14	12.90	15.58	1.56	20.84	2.35	0.29	3.81
Ti	9.56	3.87	9.00	1.40	10.93	3.01	0.99	8.28
SS	14.62	1.86	13.11	1.14	17.95	5.21	1.34	21.76
Ti6Al4V	15.24	9.46	13.38	1.61	37.20	4.44	0.33	3.95
Inconel	14.56	2.97	12.47	1.14	16.17	5.76	1.26	18.00

3.4.2 Particle size distribution fitting models for ultrasonic atomized produced powder

Figure 3.11 shows how different PSD models were able to accurately fit the reported volume-based size distributions of metal particles(AlSi12). These models include normal, log-normal, Rosin-Rammler, and Nukiyama-Tanasawa. Table 3.9 provides a summary of the parameters that fit each metal powder and model type the best. It is clear that the normal and Rosin-Rammler distribution models do not suit the actual data as well as the Nukiyama-Tanasawa and log-normal distributions do.

Figure 3.12 shows how PSD models were used to match the measured number-based size distributions of metal powders. Table 3.10 compiles the matching best-fitted model parameters. The Rosin Rammler model is best suited to describe the PSDs of AlSi12 at all angle of manipulator.

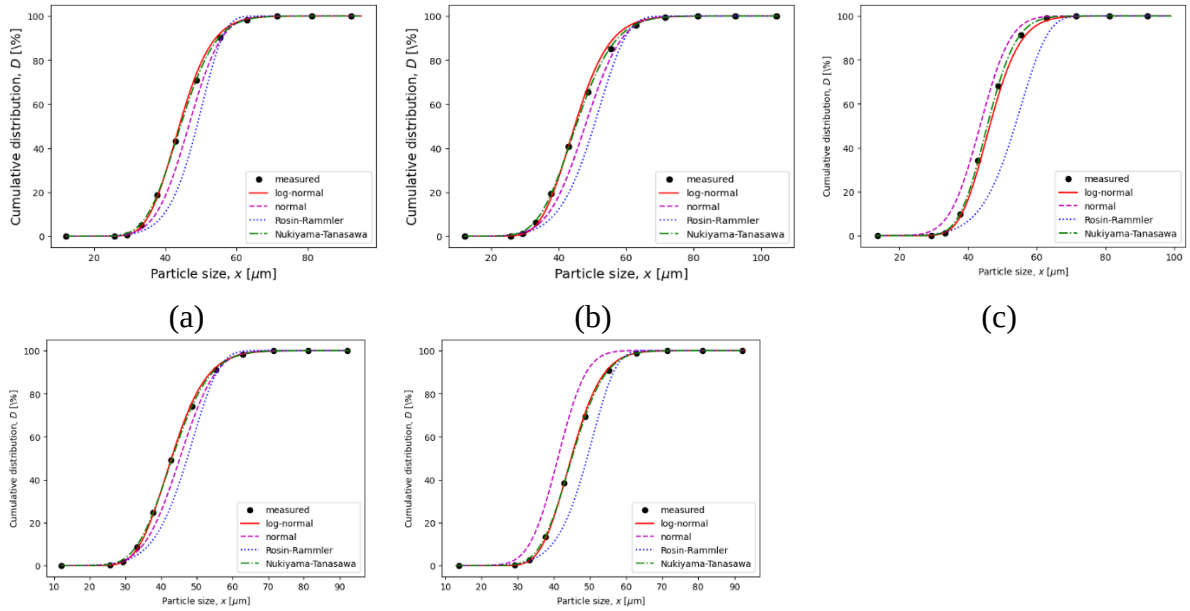

(a) (b) (c)

(d) (e)

Figure 3.11 Fitting of volume-based PSDs with normal, log-normal, Rosin-Rammler and Nukiyama Tanasawa distributions: (a) AlSi12(0), (b) AlSi12(2.5), (c) AlSi12(-2.5), (d) AlSi12(5), (e) AlSi12(-5)

Table 3.9 Parameters of best-fitted volume-based PSD models.

Metal powder	Normal		Log-normal		Rosin-Rammler		Nukiyama	
	x_m	Σ	x_g	σ_g	x_e	N	B	P
AlSi12(0°)	46.55	7.24	43.91	1.18	50.92	8.93	0.74	31.90
AlSi12(2.5°)	47.79	8.63	44.71	1.20	53.05	7.20	0.56	24.69
AlSi12(-2.5°)	43.48	7.00	46.29	1.16	56.22	7.87	1.05	47.15
AlSi12(5°)	45.27	7.93	45.91	1.20	49.73	7.44	0.64	27.05
AlSi12(-5°)	41.16	6.16	44.82	1.16	51.36	8.64	0.89	39.55

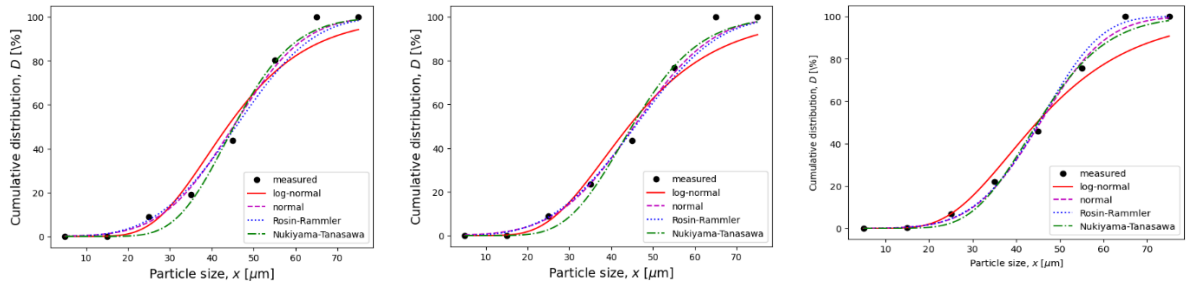

(a) (b) (c)

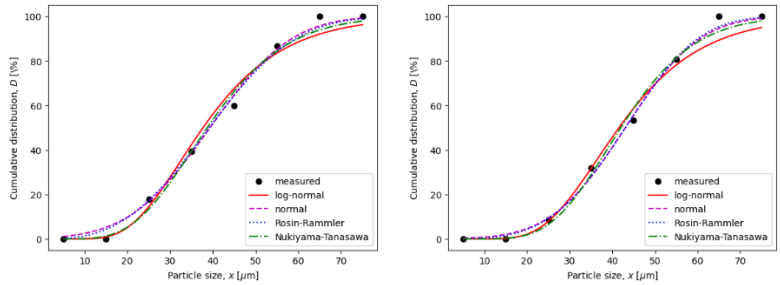

(d) (e)

Figure 3.12 Fitting of number-based PSDs with normal, log-normal, Rosin-Rammler and Nukiyama Tanasawa distributions: (a) AlSi12(0), (b) AlSi12(2.5), (c) AlSi12(-2.5), (d) AlSi12(5), (e) AlSi12(-5)

Table 3.10 Parameters of best-fitted number-based PSD models

Metal powder	Normal		Log-normal		Rosin-Rammler		Nukiyama	
	x_m	Σ	x_g	σ_g	x_e	N	b	p
AlSi12(0°)	45.10	13.31	43.74	1.41	50.65	3.60	0.37	15.89
AlSi12(2.5°)	45.50	14.61	44.23	1.46	51.02	3.39	0.29	12.23
AlSi12(-2.5°)	45.54	12.02	44.78	1.48	49.09	4.56	0.30	12.79
AlSi12(5°)	39.36	14.95	37.72	1.47	44.50	2.88	0.19	6.66
AlSi12(-5°)	43.07	13.71	41.59	1.43	47.71	3.61	0.24	9.24

3.4.3 Statistical analysis of PSD models for commercially produced powder

Figures 3.13(a) and 3.13(b) respectively display the corrected coefficients of determination for PSD models fitted to volume- and number-based cumulative size distributions of metal particles (commercially). The findings showed that for the volume-based size distributions of all metal powders, the adjusted coefficients of determination of the PSD models, which represent the quality of fit while taking into account the number of degrees of freedom utilized, rise in the following sequences: Nukiyama-Tanasawa, Rosin-Rammler, and Normal. This pattern was also seen for the size distributions of Ti, titanium alloys, and aluminum alloys depending on numbers. The order was instead log-normal, normal, Rosin-Rammler Nukiyama-Tanasawa for the number-based size distributions of stainless steel and Inconel powders.

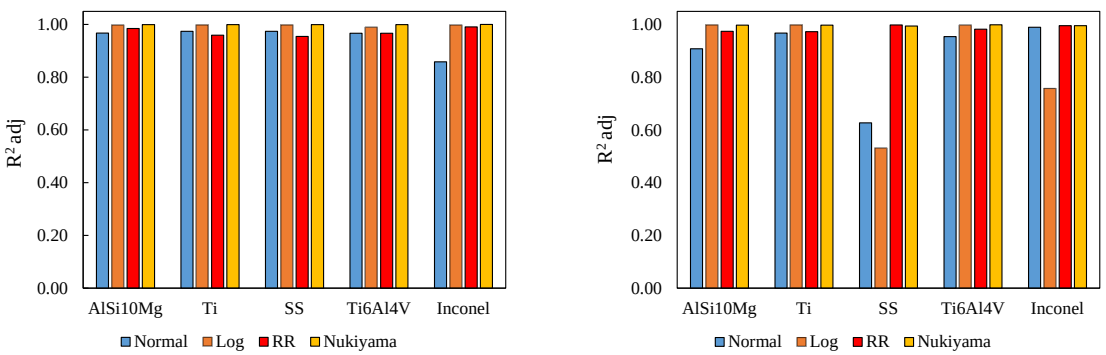

(a) (b)

Figure 3.13 Adjusted R^2 coefficients of determination for (a) volume- and (b) number-based PSD models.

Figure 3.14 displays the root mean square errors for PSD models of metal particles. The Nukiyama-Tanasawa distribution model regularly displays the lowest RMSE value among models for volume-based size distributions, demonstrating that it can more precisely fit measured size distributions than the log-normal, normal, and Rosin-Rammler models. For number-based size distributions, the Nukiyama-Tanasawa model is the best match for the remaining powders, while the log-normal model exhibits the lowest RMSE values for the AlSi10Mg and Ti powders.

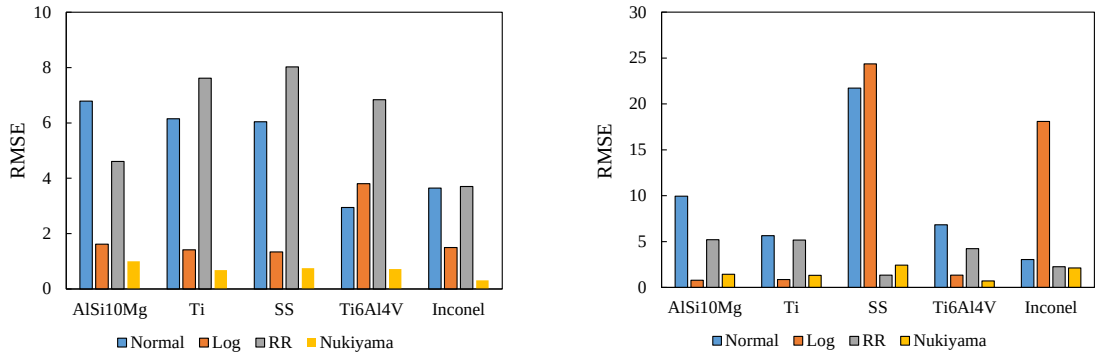

(a) (b)

Figure 3.14 Root mean square errors for (a) volume- and (b) number-based size distribution models.

Figure 3.15 displays the updated metrics for the Akaike Information Criterion for four models of the size distributions of metal particles. The volume-based distributions model proposed by Nukiyama-Tanasawa has the lowest corrected AIC value, which indicates that it is the most effective model among those examined in this study, according to the results. For number-based distributions, the Nukiyama-Tanasawa model for the remaining powders has the lowest corrected AIC value, while the log-normal model has the lowest corrected AIC value for AlSi10Mg and Ti.

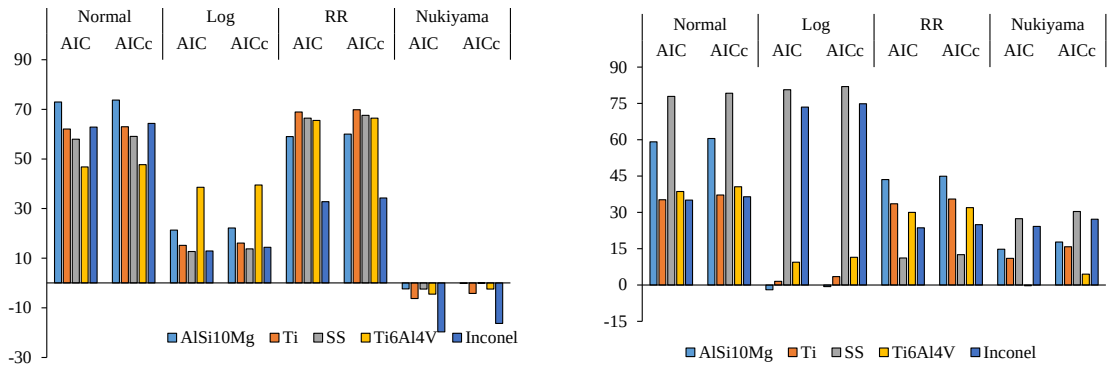

(a) (b)

Figure 3.15 AIC and AICcorrected for (a) volume- and (b) number-based size distribution models.

3.4.4 Statistical analysis of PSD models for ultrasonic atomized produced powder

Figures 3.16(a) and (b) respectively display the corrected coefficients of determination for PSD models fitted to volume- and number-based cumulative size distributions of metal particles (AlSi12). The findings showed that for the volume-based size distributions of all metal powders, the adjusted coefficients of determination of the PSD models, which represent the quality of fit Nukiyama-Tanasawa model. For the number based, Rosin Rammler showed the best fit model for powder AlSi12 produced at angle 2.5°,-2.5°,5°,-5° expect at angle 0°.

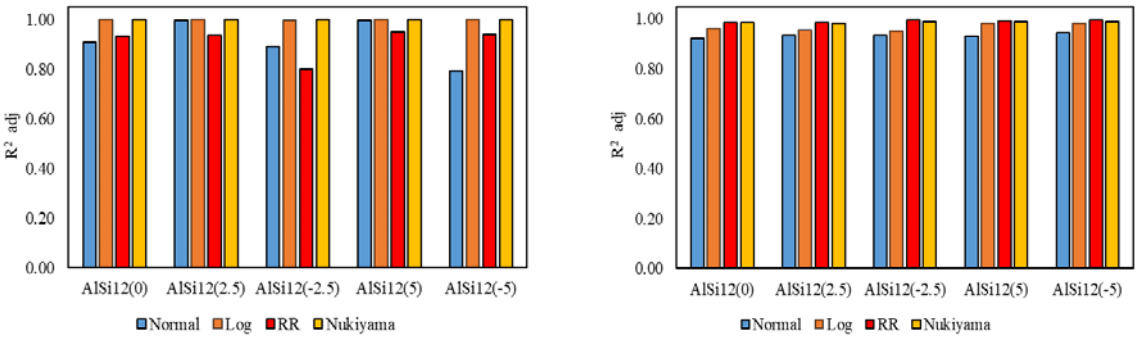

(a) (b)

Figure 3.16 Adjusted coefficients R2of determination for (a) volume- and (b) number-based PSD models.

Figure 3.17 displays the root mean square errors for PSD models of metal particles. The Nukiyama-Tanasawa distribution model regularly displays the lowest RMSE value among models for volume-based size distributions, demonstrating that it can more precisely fit measured size distributions than the log-normal, normal, and Rosin-Rammler models. For the

number based, Rosin Rammler showed the best fit model for powder AlSi12 produced at angle 2.5°,-2.5°,5°,-5° expect at angle 0°.

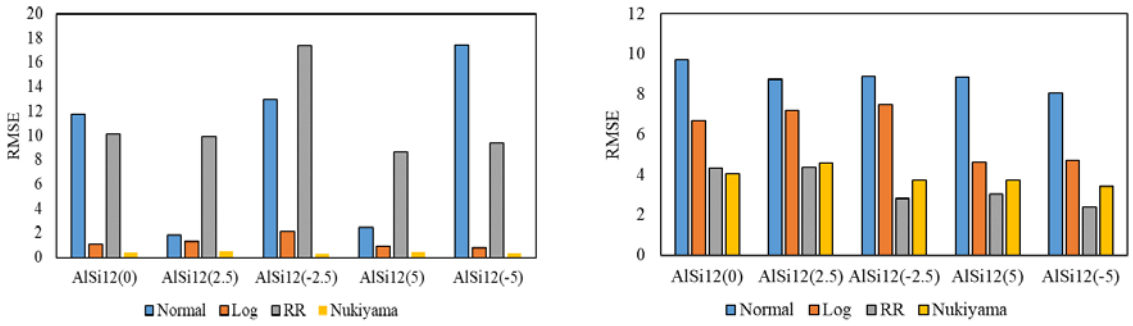

(a) (b)

Figure 3. 17 Root mean square errors for (a) volume- and (b) number-based size distribution models.

Figure 3.18 displays the updated metrics for the Akaike Information Criterion for four models of the size distributions of metal particles. The volume-based distributions model proposed by Nukiyama-Tanasawa has the lowest corrected AIC value, which indicates that it is the most effective model among those examined in this study, according to the results. For the number based, Rosin Rammler showed the lowest value for powder AlSi12 produced at angle 2.5°,-2.5°,5°,-5° expect at angle 0°.

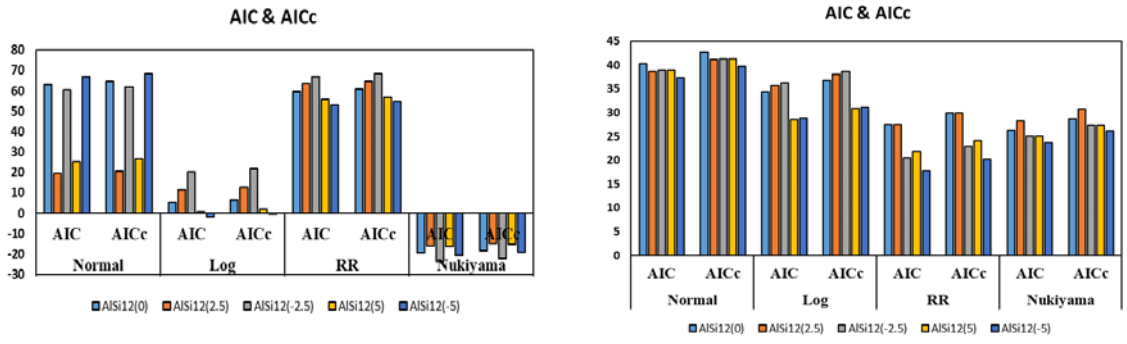

(a) (b)

Figure 3.18 AIC and AICcorrected for (a) volume- and (b) number-based size distribution models.

3.5 Hausner Ratio and Carr Index for flowability

3.5.1 Hausner Ratio and Carr Index for Commercially produced powder and ultrasonic atomized powder AlSi12

To measure flowability of metal powder, tapped density and bulk density is measured

using Hall flow meter and tapped density meter. Based on tapped density and bulk density, we calculate Hausner ratio and Carr index

$$Hausner\ ratio = \frac{\rho_{tapped}}{\rho_{bulk}} \tag{18}$$

$$Carr\ index = \frac{\rho_{tapped} - \rho_{bulk}}{\rho_{tapped}} \tag{19}$$

Table 3.10 shows the Hausner's ratio and Carr's index for all the commercially produced powder. Based on Hausner's ratio and Carr's index AlSI12 and Inconel-718 show excellent flowability and AlSI10Mg, Ti and Ti6Al4V shows good flowabilty. Stainless steel is less flowable among all the powders.

Table 3.11 Hausner Ratio and Carr Index for flowability of metal powders

	Bulk Density	**Tap Density**	**Hausner Ratio (HR)**	**Carr Index(CI)**	**Description of flow**
AlSi12	1.415	1.455	1.028	2.749	Excellent / Very Free Flow
AlSi10Mg	1.371	1.578	1.151	13.118	Good / Free Flow
Inconnel-718	4.788	5.1982	1.086	7.891	Excellent / Very Free Flow
Stainless Steel	4.442	5.628	1.267	21.073	Passable
Titainum	2.574	2.864	1.113	10.126	Good / Free Flow
Ti6Al4V	2.542	2.837	1.116	10.398	Good / Free Flow

3.6 Additive manufacturing suitability factor for LBFP Process

3.6.1 Additive manufacturing suitability factor of commercially produced powder and ultrasonic atomized powder AlSi12

AM Suitability factor is calculated as [55].

$$\textbf{Rheological Score/AMS} = \frac{(1/\rho_c + CI + PD + SE + AE + BFE + C)}{7}$$

where ρ_c is the conditioned bulk density; CI, the compressibility index; PD, the pressure drop; SE, the specific energy; AE, the aeration energy; BFE, the basic flow energy, and c, the cohesion coefficient. The following data was obtained from the rheometer's various tests (shear cell test, permeability, compressibility, aeration, stability, and flow rate).

Table 3.12 represents the summary of rheological properties of six powders after normalizing. The rheological properties are presented in the table 3.12. AlSi12 has a lower BEF value than other metal powders, which results in greater flowability and a reduced energy requirement for the blade. Because stainless steel has a higher BEF value, a lot of energy is

needed for the blade to go through the bed powder. AlSi10Mg has a somewhat higher specific energy and the mechanical interlocking and friction are moderately high. A more effective packing state of the metal powder is also demonstrated by the inconel, which exhibit a greater conditioned bulk density, a lower compressibility index, and titanium shows the higher pressure drop. The greatest value of aeration energy was found for the inconel. The aeration energy measures the energy required to overcome mechanically interlocking and cohesion forces. The powder which has high cohesion value and low flow function value is more flowable. Among all the powders titanium has high cohesion value and low flow function value, so it is more flowable.

The smaller the AMS, the more suitable the powder is for the AM process. Among all the powder Inconel has low score value.

Table 3.12 Summary of rheological properties of metal powder

	AlSi10Mg	**Ti**	**Ti6Al4**	**SS**	**Inconel**	**AlSi12**
BFE (mJ)	249	355	312	686	561	220
SE (mJ/g)	2.91	2.17	2.05	2.05	1.34	2.4
ρ_c(g/cm3)	1.62	2.71	2.55	4.56	4.92	1.42
CI(%)	2.03	2.97	1.93	2.07	1.55	2.64
PD(mBar)	3.86	8.77	5.59	5.92	6.13	2.65
AE(mJ)	28.7	21.9	13.9	50.5	52.8	3.78
c(kPa)	0.29	0.37	0.33	0.13	0.18	0.17

Table 3.13 Summary of rheological properties after normalizing

	AlSi10Mg	**Ti**	**Ti6Al4**	**SS**	**Inconel**	**AlSi12**
BFE (mJ)	0.36	0.52	0.45	1.00	0.82	0.32
SE (mJ/g)	1.00	0.75	0.70	0.70	0.46	0.82
ρ_c(g/cm3)	0.33	0.55	0.52	0.93	1.00	0.29
CI(%)	0.68	1.00	0.65	0.70	0.52	0.89
PD(mBar)	0.44	1.00	0.64	0.68	0.70	0.30
AE(mJ)	0.54	0.41	0.26	0.96	1.00	0.07
c(kPa)	0.78	1.00	0.89	0.35	0.49	0.46

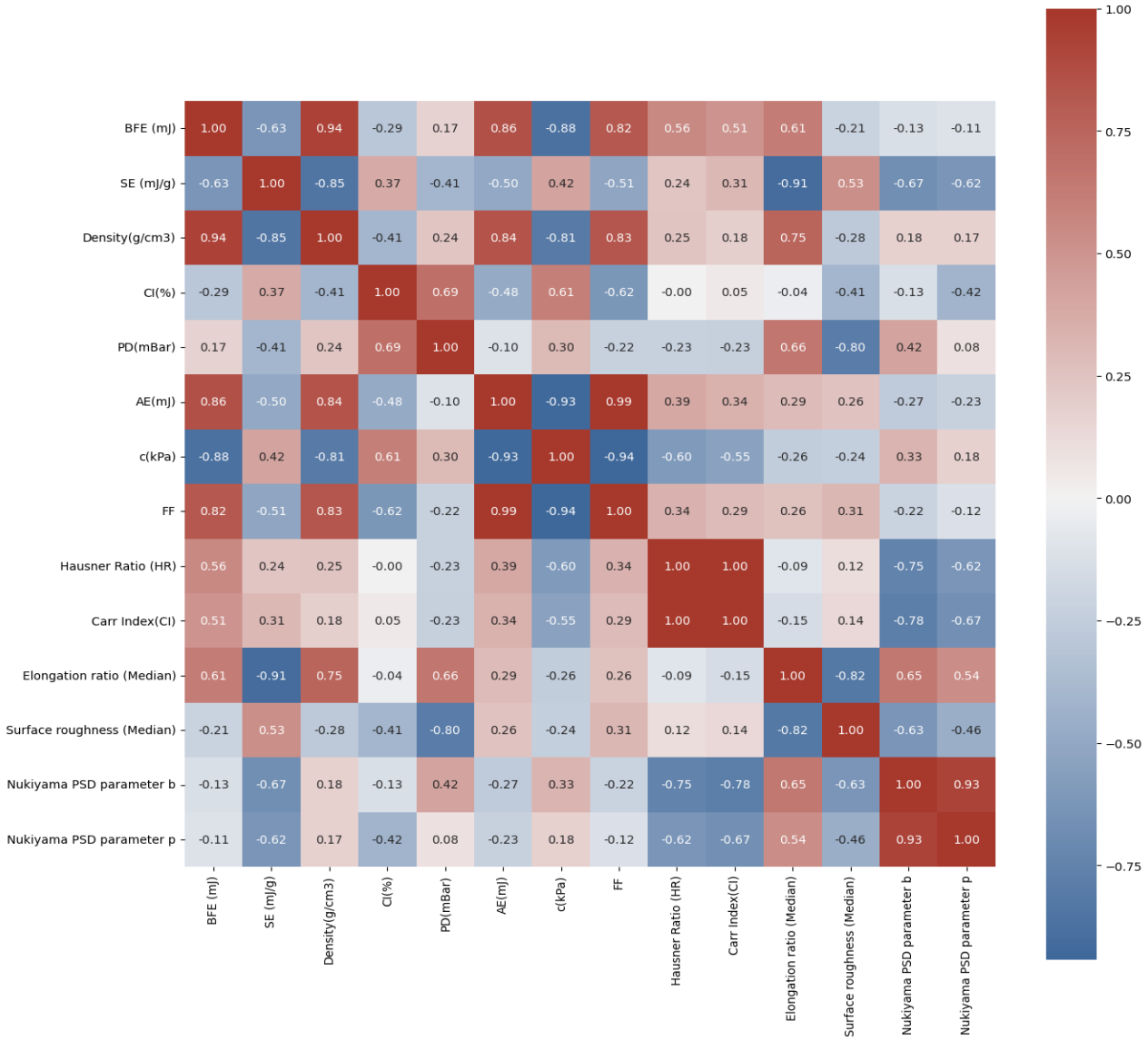

Figure 3.19 Spearman correlation coefficients between powder characteristics, including volume-based PSD parameters

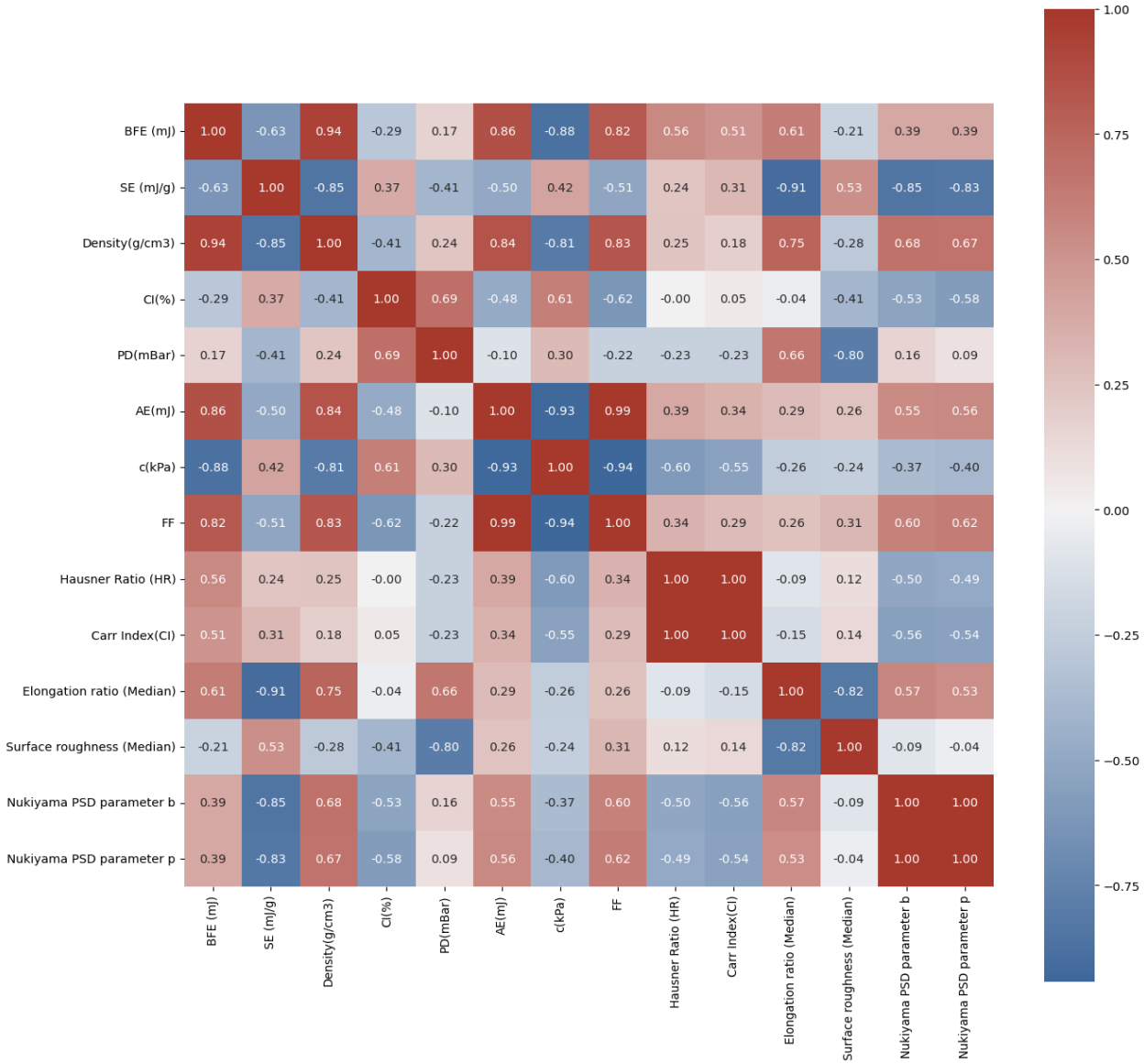

Figure 3.20 Spearman correlation coefficients between powder characteristics, including number-based PSD parameters

According to Spearman's correlation analysis, there are strong correlations between metal powders' shape and PSD model parameters and the parameters related to powder flowability, as shown in figure. 3.19 and 3.20 for volume- and number-based PSD parameters, respectively. The elongation ratio is found to be correlated with the PSD parameters and surface roughness. Furthermore, the Nukiyama model coefficients for volume-based measurements show correlations with the elongation ratio, Hausner's ratio, Carr index, density, specific energy, and flow function. Similarly, the Nukiyama model coefficients for number-based measurements are correlated with the elongation ratio, Hausner's ratio, Carr index, and surface

roughness.

The FT4 indices that characterize powder flowability strongly correlate with shape indices and PSD parameters. In contrast, Hausner's ratio and Carr index, commonly used to measure flowability, only correlate with PSD parameters and not with shape indices. The lack of influence of particle shape indices on powder flowability could be attributed to the limitations of the measuring procedures based on the funnel flow method, as they are unable to detect differences caused by slight variations in particle shape. However, more precise measurements using various procedures with the FT4 rheometer make it possible to detect the correlation between FT4 indices and shape indices. The elongation ratio strongly correlates to SE, conditioned bulk density, BPE, and PD, and the surface ratio to PD and SE.

Chapter 4- Conclusions

In this study, we aimed to characterize the size distribution and morphology of commonly used powders in additive manufacturing, including AlSi10Mg, Inconel-718, Ti6Al4V, titanium, and stainless steel and ultrasonic atomized powder AlSi12. We applied several PSD models, namely normal, log-normal, Rosin-Rammler, and Nukiyama-Tanasawa, to fit the measured volume- and number-based size distributions. To determine the best-fitting PSD models, we conducted a statistical analysis using adjusted R^2, root mean square error, and corrected Akaike's information criterion. In addition, we employed shape analysis of SEM images to quantitatively characterize the particle morphology, using the elliptic Fourier series to derive shape indices and FT-4 rheometer, Hausner;s Ratio and Carr Index to measure the flowability.

Based on the data and analyses presented, we draw the following conclusions:

1. AlSi10Mg powder exhibits the widest size distribution in terms of both volume and number and has the largest median size based on volume and the second largest median size based on number. In contrast, Inconel-718 and stainless-steel powders exhibit the narrowest volume- and number-based PSDs. Additionally, titanium powder has the smallest median sizes. The ultrasonic atomized AlSi12 powder produced at an angle of 2.5° has the widest particle size dispersion in terms of volume while AlSi12 powder produced at an angle 5° in term of number, according to the data. The narrowest volume- and number-based particle size distributions, however, are shown by AlSi12 powder produced at angle -2.5°and AlSi12 powder produced at angle 0°, respectively.
2. The metal particles, except for AlSi10Mg, are nearly spherical, with elongation ratios ranging from 0.90 to 1 and a median elongation ratio greater than 0.96. In particular, Inconel-718 particles have the highest level of sphericity, with a median elongation ratio of 0.99 and a narrow distribution. However, alumina alloy particles exhibit a wide range of elongation ratios, indicating the presence of agglomerated particles with various shapes. AlSi10Mg particles have the roughest surface structure, while Ti particles have the smoothest surface. Most metal particles of AlSi12, have an elongation ratio (ER) ranging from 0.90 to 1. AlSi12 particles produced at angle -5 show the highest level of sphericity, with a median ER of 0.99 and a narrow ER distribution.
3. The Nukiyama-Tanasawa and log-normal distributions provide a better fit to experimental data than the normal and Rosin-Rammler distribution models when fitting PSD models to

volume-based size distributions of metal particles. Additionally, the log-normal model accurately fits the number-based PSD of AlSi10Mg and Ti powders, while the Nukiyama-Tanasawa model is better suited for describing the PSDs of Ti6Al4V, Inconel-718, and stainless steel powders. The Nukiyama-Tanasawa model is well-suited for describing the size distribution of metal powders that are prepared by the atomization of molten metals. For ultrasonic atomized powder AlSI12 normal and Rosin-Rammler distribution models do not suit the actual data as well as the Nukiyama-Tanasawa and log-normal distributions do.The Rosin Rammler model is best suited to describe the PSDs of AlSi12 at all angle of manipulator.

4. Inconel-718 powder has exceptional flowability, AlSi12, AlSi10Mg, Ti, and Ti6Al4V exhibit good flowability, and stainless steel shows the lowest flowability among the tested metal powder based on Hausner's ratio and Carr index. Powder rheology tests using FT4 rheometer indicate that AlSi12 has the lowest BEF value, resulting in good flowability, Inconel-718 powder forms a denser bed, and titanium has the highest cohesion value and the lowest flow function value, making it the most flowable among all the powders tested.
5. Strong correlations were observed between metal powders' shape and PSD model parameters and the parameters related to powder flowability based on Spearman's correlation analysis.

The process of ultrasonic atomization is being studied by researchers to optimize it for AM applications. This includes refining the size and shape of powder particles, as well as increasing production rates and decreasing energy consumption. Furthermore, new materials are being researched for use in ultrasonic atomization, such as high-temperature alloys and refractory metals, which are ideal for AM applications. The development of metal powders and ultrasonic atomized powder in AM is anticipated to produce more intricate and functional parts with enhanced properties, expanding the range of applications in sectors such as aerospace, automotive, and biomedical.

References

[1] K. Kassym and A. Perveen, “Atomization processes of metal powders for 3D printing,” *Mater Today Proc*, vol. 26, pp. 1727–1733, Jan. 2020, doi: 10.1016/J.MATPR.2020.02.364.

[2] B. E. Carroll, T. A. Palmer, and A. M. Beese, “Anisotropic tensile behavior of Ti–6Al–4V components fabricated with directed energy deposition additive manufacturing,” *Acta Mater*, vol. 87, pp. 309–320, Apr. 2015, doi: 10.1016/J.ACTAMAT.2014.12.054.

[3] E. Brandl, F. Palm, V. Michailov, B. Viehweger, and C. Leyens, “Mechanical properties of additive manufactured titanium (Ti–6Al–4V) blocks deposited by a solid-state laser and wire,” *Mater Des*, vol. 32, no. 10, pp. 4665–4675, Dec. 2011, doi: 10.1016/J.MATDES.2011.06.062.

[4] L. V. M. Antony and R. G. Reddy, “Processes for production of high-purity metal powders,” *JOM*, vol. 55, no. 3, pp. 14–18, 2003, doi: 10.1007/S11837-003-0153-4/METRICS.

[5] Ł. Żrodowski *et al.*, “Novel Cold Crucible Ultrasonic Atomization Powder Production Method for 3D Printing,” *Materials 2021, Vol. 14, Page 2541*, vol. 14, no. 10, p. 2541, May 2021, doi: 10.3390/MA14102541.

[6] L. E. Murr *et al.*, “Fabrication of Metal and Alloy Components by Additive Manufacturing: Examples of 3D Materials Science,” *Journal of Materials Research and Technology*, vol. 1, no. 1, pp. 42–54, Apr. 2012, doi: 10.1016/S2238-7854(12)70009-1.

[7] S. Cooke, K. Ahmadi, S. Willerth, and R. Herring, “Metal additive manufacturing: Technology, metallurgy and modelling,” *J Manuf Process*, vol. 57, pp. 978–1003, Sep. 2020, doi: 10.1016/J.JMAPRO.2020.07.025.

[8] S. Cooke, K. Ahmadi, S. Willerth, and R. Herring, “Metal additive manufacturing: Technology, metallurgy and modelling,” *J Manuf Process*, vol. 57, pp. 978–1003, Sep. 2020, doi: 10.1016/J.JMAPRO.2020.07.025.

[9] T. S. Jang, D. E. Kim, G. Han, C. B. Yoon, and H. Do Jung, “Powder based additive manufacturing for biomedical application of titanium and its alloys: a review,” *Biomed Eng Lett*, vol. 10, no. 4, pp. 505–516, Nov. 2020, doi: 10.1007/S13534-020-00177-2/METRICS.

[10] M. Mehrabi, J. Gardy, F. A. Talebi, A. Farshchi, A. Hassanpour, and A. E. Bayly, “An investigation of the effect of powder flowability on the powder spreading in additive manufacturing,” *Powder Technol*, vol. 413, p. 117997, Jan. 2023, doi: 10.1016/J.POWTEC.2022.117997.

[11] S. Vock, B. Klöden, A. Kirchner, T. Weißgärber, and B. Kieback, “Powders for powder bed fusion: a review,” *Progress in Additive Manufacturing*, vol. 4, no. 4, pp. 383–397, Dec. 2019, doi: 10.1007/S40964-019-00078-6/TABLES/3.

[12] A. B. Spierings, M. Voegtlin, T. Bauer, and K. Wegener, “Powder flowability characterisation methodology for powder-bed-based metal additive manufacturing,” *Progress in Additive Manufacturing*, vol. 1, no. 1–2, pp. 9–20, Jun. 2016, doi: 10.1007/S40964-015-0001-4/FIGURES/12.

[13] J. Zegzulka, D. Gelnar, L. Jezerska, R. Prokes, and J. Rozbroj, “Characterization and flowability methods for metal powders,” 2020, doi: 10.1038/s41598-020-77974-3.

[14] G. Miao, W. Du, Z. Pei, and C. Ma, “A literature review on powder spreading in additive manufacturing,” *Addit Manuf*, vol. 58, p. 103029, Oct. 2022, doi: 10.1016/J.ADDMA.2022.103029.

[15] I. E. Anderson, E. M. H. White, and R. Dehoff, “Feedstock powder processing research needs for additive manufacturing development,” *Curr Opin Solid State Mater Sci*, vol. 22, no. 1, pp. 8–15, Feb. 2018, doi: 10.1016/J.COSSMS.2018.01.002.

[16] K. Grzelak *et al.*, “A Comparative Study on Laser Powder Bed Fusion of Differently Atomized 316L Stainless Steel,” *Materials 2022, Vol. 15, Page 4938*, vol. 15, no. 14, p. 4938, Jul. 2022, doi: 10.3390/MA15144938.
[17] M. Habibnejad-korayem, J. Zhang, and Y. Zou, “Effect of particle size distribution on the flowability of plasma atomized Ti-6Al-4V powders,” *Powder Technol*, vol. 392, pp. 536–543, Nov. 2021, doi: 10.1016/J.POWTEC.2021.07.026.
[18] J. Dawes, R. Bowerman, and R. Trepleton, “Introduction to the additive manufacturing powder metallurgy supply chain,” *Johnson Matthey Technology Review*, vol. 59, no. 3, pp. 243–256, 2015, doi: 10.1595/205651315X688686.
[19] M. J. Tobar, J. M. Amado, J. Montero, and A. Yáñez, “A Study on the Effects of the Use of Gas or Water Atomized AISI 316L Steel Powder on the Corrosion Resistance of Laser Deposited Material,” *Phys Procedia*, vol. 83, pp. 606–612, Jan. 2016, doi: 10.1016/J.PHPRO.2016.08.063.
[20] P. Avrampos and G. C. Vosniakos, “A review of powder deposition in additive manufacturing by powder bed fusion,” *J Manuf Process*, vol. 74, pp. 332–352, Feb. 2022, doi: 10.1016/J.JMAPRO.2021.12.021.
[21] K. Kikuchi, Y. Tanifuji, W. Zhou, N. Nomura, and A. Kawasaki, “Experimental Characterization and Computational Simulation of Powder Bed for Powder Bed Fusion Additive Manufacturing,” *Mater Trans*, vol. 63, no. 6, pp. 931–938, Jun. 2022, doi: 10.2320/MATERTRANS.MT-Y2021005.
[22] R. Groarke *et al.*, “316L Stainless Steel Powders for Additive Manufacturing: Relationships of Powder Rheology, Size, Size Distribution to Part Properties,” *Materials 2020, Vol. 13, Page 5537*, vol. 13, no. 23, p. 5537, Dec. 2020, doi: 10.3390/MA13235537.
[23] A. Averardi, C. Cola, S. E. Zeltmann, and N. Gupta, “Effect of particle size distribution on the packing of powder beds: A critical discussion relevant to additive manufacturing,” *Mater Today Commun*, vol. 24, p. 100964, Sep. 2020, doi: 10.1016/J.MTCOMM.2020.100964.
[24] Y. Huang, M. B. Khamesee, and E. Toyserkani, “A comprehensive analytical model for laser powder-fed additive manufacturing,” *Addit Manuf*, vol. 12, pp. 90–99, Oct. 2016, doi: 10.1016/J.ADDMA.2016.07.001.
[25] V. Seyda, D. Herzog, and C. Emmelmann, “Relationship between powder characteristics and part properties in laser beam melting of Ti–6Al–4V, and implications on quality,” *J Laser Appl*, vol. 29, no. 2, p. 022311, Jun. 2017, doi: 10.2351/1.4983240.
[26] C. Vipulanandan, M. Asce, and H. Gurkan Ozgurel, “Simplified Relationships for Particle-Size Distribution and Permeation Groutability Limits for Soils,” *Journal of Geotechnical and Geoenvironmental Engineering*, vol. 135, no. 9, pp. 1190–1197, Feb. 2009, doi: 10.1061/(ASCE)GT.1943-5606.0000064.
[27] H. Bayat, M. Rastgou, A. Nemes, M. Mansourizadeh, and P. Zamani, “Mathematical models for soil particle-size distribution and their overall and fraction-wise fitting to measurements,” *Eur J Soil Sci*, vol. 68, no. 3, pp. 345–364, May 2017, doi: 10.1111/EJSS.12423.
[28] L. Colorado-Arango, J. M. Menéndez-Aguado, and A. Osorio-Correa, “Particle size distribution models for metallurgical coke grinding products,” *Metals (Basel)*, vol. 11, no. 8, p. 1288, Aug. 2021, doi: 10.3390/MET11081288/S1.
[29] C. Meier, R. Weissbach, J. Weinberg, W. A. Wall, and A. J. Hart, “Critical influences of particle size and adhesion on the powder layer uniformity in metal additive manufacturing,” *J Mater Process Technol*, vol. 266, pp. 484–501, Apr. 2019, doi: 10.1016/J.JMATPROTEC.2018.10.037.
[30] Y. Liu, X. H. Zhao, Y. J. Lai, Q. X. Wang, L. M. Lei, and S. J. Liang, “A brief

introduction to the selective laser melting of Ti6Al4V powders by supreme-speed plasma rotating electrode process," *Progress in Natural Science: Materials International*, vol. 30, no. 1, pp. 94–99, Feb. 2020, doi: 10.1016/J.PNSC.2019.12.004.

[31] Z. Y. Han *et al.*, "Morphology and particle analysis of the Ni3Al-based spherical powders manufactured by supreme-speed plasma rotating electrode process," *Journal of Materials Research and Technology*, vol. 9, no. 6, pp. 13937–13944, Nov. 2020, doi: 10.1016/J.JMRT.2020.09.102.

[32] S. A. Farzadfar, M. J. Murtagh, and N. Venugopal, "Impact of IN718 bimodal powder size distribution on the performance and productivity of laser powder bed fusion additive manufacturing process," *Powder Technol*, vol. 375, pp. 60–80, Sep. 2020, doi: 10.1016/J.POWTEC.2020.07.092.

[33] P. Kiani, U. Scipioni Bertoli, A. D. Dupuy, K. Ma, and J. M. Schoenung, "A Statistical Analysis of Powder Flowability in Metal Additive Manufacturing," *Adv Eng Mater*, vol. 22, no. 10, p. 2000022, Oct. 2020, doi: 10.1002/ADEM.202000022.

[34] A. Mussatto, R. Groarke, A. O'Neill, M. A. Obeidi, Y. Delaure, and D. Brabazon, "Influences of powder morphology and spreading parameters on the powder bed topography uniformity in powder bed fusion metal additive manufacturing," *Addit Manuf*, vol. 38, p. 101807, Feb. 2021, doi: 10.1016/J.ADDMA.2020.101807.

[35] Y. Zhao, B. Yu, G. Yu, and W. Li, "Study on the water-heat coupled phenomena in thawing frozen soil around a buried oil pipeline," *Appl Therm Eng*, vol. 73, no. 2, pp. 1477–1488, Dec. 2014, doi: 10.1016/J.APPLTHERMALENG.2014.06.017.

[36] P. Muthuswamy, "Influence of powder characteristics on properties of parts manufactured by metal additive manufacturing," *Lasers in Manufacturing and Materials Processing*, vol. 9, no. 3, pp. 312–337, Sep. 2022, doi: 10.1007/S40516-022-00177-3/METRICS.

[37] L. Xiong *et al.*, "Defect and satellite characteristics of additive manufacturing metal powders," *Advanced Powder Technology*, vol. 33, no. 3, p. 103486, Mar. 2022, doi: 10.1016/J.APT.2022.103486.

[38] A. Nouri and A. Sola, "Metal particle shape: A practical perspective," *Metal Powder Report*, vol. 73, no. 5, pp. 276–282, Sep. 2018, doi: 10.1016/J.MPRP.2018.04.001.

[39] L. C. Zhang, W. Y. Xu, Z. Li, L. Zheng, Y. F. Liu, and G. Q. Zhang, "Characterization of particle shape of nickel-based superalloy powders using image processing techniques," *Powder Technol*, vol. 395, pp. 787–801, Jan. 2022, doi: 10.1016/J.POWTEC.2021.10.013.

[40] T. Ueda, "Reproducibility of the repose angle, porosity, and coordination number of particles generated by spherical harmonic-based principal component analysis using discrete element simulation," *Powder Technol*, vol. 415, p. 118143, Feb. 2023, doi: 10.1016/J.POWTEC.2022.118143.

[41] K. Shinohara, M. Oida, and B. Golman, "Effect of particle shape on angle of internal friction by triaxial compression test," *Powder Technol*, vol. 107, no. 1–2, pp. 131–136, Jan. 2000, doi: 10.1016/S0032-5910(99)00179-5.

[42] P. M. Raj and W. R. Cannon, "2-D particle shape averaging and comparison using Fourier descriptors," *Powder Technol*, vol. 104, no. 2, pp. 180–189, Sep. 1999, doi: 10.1016/S0032-5910(99)00046-7.

[43] T. Shibata, B. Golman, K. Shinohara, M. Otani, and T. Uchiyama, "Profile analysis of surfaces lapped with diamond particles of several shapes," *Wear*, vol. 254, no. 7–8, pp. 742–748, Apr. 2003, doi: 10.1016/S0043-1648(03)00251-5.

[44] C. A. Schneider, W. S. Rasband, and K. W. Eliceiri, "NIH Image to ImageJ: 25 years of image analysis," *Nature Methods 2012 9:7*, vol. 9, no. 7, pp. 671–675, Jun. 2012, doi: 10.1038/nmeth.2089.

[45] T. Shibata, B. Golman, K. Shinohara, M. Otani, and T. Uchiyama, “Profile analysis of surfaces lapped with diamond particles of several shapes,” *Wear*, vol. 254, no. 7–8, pp. 742–748, Apr. 2003, doi: 10.1016/S0043-1648(03)00251-5.

[46] T. Ueda, “Reproducibility of the repose angle, porosity, and coordination number of particles generated by spherical harmonic-based principal component analysis using discrete element simulation,” *Powder Technol*, vol. 415, p. 118143, Feb. 2023, doi: 10.1016/J.POWTEC.2022.118143.

[47] K. Shinohara, M. Oida, and B. Golman, “Effect of particle shape on angle of internal friction by triaxial compression test,” *Powder Technol*, vol. 107, no. 1–2, pp. 131–136, Jan. 2000, doi: 10.1016/S0032-5910(99)00179-5.

[48] N. S, “Experiments on the atomization of liquids in an air stream, report 3, on the droplet-size distribution in a atomized jet,” *Trans. Soc. Mech. Eng. Japan*, vol. 5, pp. 62–67, 1939, Accessed: Mar. 19, 2023. [Online]. Available: https://cir.nii.ac.jp/crid/1573387450665012480

[49] D. Chen *et al.*, “Effect of particle morphology on the flowability of HDH Ti powders treated by high temperature ball milling,” *Advanced Powder Technology*, vol. 33, no. 11, p. 103803, Nov. 2022, doi: 10.1016/J.APT.2022.103803.

[50] “Atomization and Sprays - Arthur H. Lefebvre, Vincent G. McDonell - Google Books.” https://books.google.kz/books?hl=en&lr=&id=80OEDgAAQBAJ&oi=fnd&pg=PP1&dq=Lefebvre,+A.+H.%3B+McDonell,+V.+G.+Atomization+and+Sprays,+2nd+Ed.%3B+CRC+Press:+Boca+Raton,+FL,+2017%3B+pp.+57-58&ots=i_pRUy2bco&sig=9IC5hwF9hZS0fzWD8yYgtLHQFnA&redir_esc=y#v=onepage&q&f=false (accessed Mar. 19, 2023).

[51] M. Alderliesten and M. Alderliesten, “Mean Particle Diameters. Part VII. The Rosin-Rammler Size Distribution: Physical and Mathematical Properties and Relationships to Moment-Ratio Defined Mean Particle Diameters,” *Particle & Particle Systems Characterization*, vol. 30, no. 3, pp. 244–257, Mar. 2013, doi: 10.1002/PPSC.201200021.

[52] C. A. Dunbar and A. J. Hickey, “EVALUATION OF PROBABILITY DENSITY FUNCTIONS TO APPROXIMATE PARTICLE SIZE DISTRIBUTIONS OF REPRESENTATIVE PHARMACEUTICAL AEROSOLS,” *J Aerosol Sci*, vol. 31, no. 7, pp. 813–831, Jul. 2000, doi: 10.1016/S0021-8502(99)00557-1.

[53] S. S. Yoon, “Droplet distributions at the liquid core of a turbulent spray,” *Physics of Fluids*, vol. 17, no. 3, p. 035103, Jan. 2005, doi: 10.1063/1.1852577.

[54] T. A. Reddy and C. Garlapati, “Dimensionless Empirical Model to Correlate Pharmaceutical Compound Solubility in Supercritical Carbon Dioxide,” *Chem Eng Technol*, vol. 42, no. 12, pp. 2621–2630, Dec. 2019, doi: 10.1002/CEAT.201900283.

[55] S. E. Brika, M. Letenneur, C. A. Dion, and V. Brailovski, “Influence of particle morphology and size distribution on the powder flowability and laser powder bed fusion manufacturability of Ti-6Al-4V alloy,” *Addit Manuf*, vol. 31, p. 100929, Jan. 2020, doi: 10.1016/J.ADDMA.2019.100929.